HAL
open science

ProLB: A Lattice Boltzmann Solver of Large-Eddy Simulation for Atmospheric Boundary Layer Flows

Yongliang Feng, Johann Miranda-fuentes, Shaolong Guo, Jérôme Jacob, Pierre Sagaut

▶ To cite this version:

Yongliang Feng, Johann Miranda-fuentes, Shaolong Guo, Jérôme Jacob, Pierre Sagaut. ProLB: A Lattice Boltzmann Solver of Large-Eddy Simulation for Atmospheric Boundary Layer Flows. Journal of Advances in Modeling Earth Systems, 2021, 13 (3), pp.e2020MS002107. 10.1029/2020MS002107 . hal-03326123

HAL Id: hal-03326123

https://hal.science/hal-03326123v1

Submitted on 7 Sep 2021

HAL is a multi-disciplinary open access archive for the deposit and dissemination of scientific research documents, whether they are published or not. The documents may come from teaching and research institutions in France or abroad, or from public or private research centers.

L'archive ouverte pluridisciplinaire **HAL**, est destinée au dépôt et à la diffusion de documents scientifiques de niveau recherche, publiés ou non, émanant des établissements d'enseignement et de recherche français ou étrangers, des laboratoires publics ou privés.

Distributed under a Creative Commons Attribution - NonCommercial - NoDerivatives 4.0 International License

Check for updates

AGU ADVANCING EARTH AND SPACE SCIENCE

JAMES | Journal of Advances in Modeling Earth Systems

RESEARCH ARTICLE
10.1029/2020MS002107

Key Points:

- An efficient large-eddy simulation tool within framework of lattice Boltzmann method is developed for simulating the dynamics of atmospheric boundary layers and urban flows
- Immersed boundary approach coupled with wall models is introduced to handle flows in complex configurations, with application to turbulent flows in realistic urban areas
- The basic core, wall models, subgrid models, and interaction terms are described, implemented, and assessed in various micro-meteorological flows and urban flows

Correspondence to:
P. Sagaut,
pierre.sagaut@univ-amu.fr

Citation:
Feng, Y., Miranda-Fuentes, J., Guo, S., Jacob, J., & Sagaut, P. (2021). ProLB: A lattice Boltzmann solver of large-eddy simulation for atmospheric boundary layer flows. *Journal of Advances in Modeling Earth Systems*, *13*, e2020MS002107. https://doi.org/10.1029/2020MS002107

Received 14 MAR 2020
Accepted 17 DEC 2020

© 2020. The Authors.
This is an open access article under the terms of the Creative Commons Attribution-NonCommercial-NoDerivs License, which permits use and distribution in any medium, provided the original work is properly cited, the use is non-commercial and no modifications or adaptations are made.

ProLB: A Lattice Boltzmann Solver of Large-Eddy Simulation for Atmospheric Boundary Layer Flows

Yongliang Feng[1], Johann Miranda-Fuentes[1], Shaolong Guo[1], Jérôme Jacob[1], and Pierre Sagaut[1]

[1]Aix Marseille Univ, CNRS, Centrale Marseille, M2P2 UMR 7340, Marseille, France

Abstract A large-eddy simulation tool is developed for simulating the dynamics of atmospheric boundary layers (ABLs) using lattice Boltzmann method (LBM), which is an alternative approach for computational fluid dynamics and proved to be very well suited for the simulation of low-Mach flows. The equations of motion are coupled with the global complex physical models considering the coupling among several mechanisms, namely basic hydro-thermodynamics and body forces related to stratification, Coriolis force, canopy effects, humidity transport, and condensation. Mass and momentum equations are recovered by an efficient streaming, collision, and forcing process within the framework of LBM while the governing equations of temperature, liquid, and vapor water fraction are solved using a finite volume method. The implementation of wall models for ABL, subgrid models, and interaction terms related to multiphysic phenomena (e.g., stratification, condensation) is described, implemented, and assessed in this study. An immersed boundary approach is used to handle flows in complex configurations, with application to flows in realistic urban areas. Applications to both wind engineering and atmospheric pollutant dispersion are illustrated.

Plain Language Summary We have described a new tool for large-eddy simulation (LES) of atmospheric flows in this paper. LES with the lattice Boltzmann method (LBM) was used to simulate dry and cloudy atmospheric boundary layers (ABLs), along with flows in complex urban areas. To validate our LBM-LES solver, we first simulated the four basic ABL cases coming from the previous intercomparison of LES codes. These were the neutral, convective, stable, and cloudy convective boundary layers. Then three extra cases for ABL with canopy effects were performed by our solver. The altitude-dependent drag force and heat release source term were introduced and assessed in the present solver compared reference data. At last, the ProLB tool was successfully assessed considering two urban flow configurations: wind prediction in Shinjuku district in Tokyo, and gaseous pollutant dispersion in the Champs Elysées district in Paris. In both cases, very satisfactory comparisons with experimental data were recovered.

1. Introduction

The atmospheric boundary layer (ABL) ranges from hundreds of meters to several kilometers depending on meteorological conditions, mainly wind, temperature, and humidity. Thus, structure of ABL is modified by the daily cycle of heating and cooling over Earth's surface producing three canonical types of boundary layers: convective or unstable, neutral, and stable boundary layers. Convective boundary layer is commonly observed during day when the surface is heated by the sun resulting in a positive buoyancy force, while stable boundary layer occurs during night when surface is cooled by radiation producing a negative buoyancy force, and neutral boundary layer is the case between the former two with little or no buoyancy.

The structure of ABL has an important effect on anthropic activities such as mesoscale weather forecasting or pollutant dispersion in urban areas (Fernando et al., 2001). To better understand ABL and related urban processes, numerical simulation is a good complement to field measurements and wind tunnel experiments (Blocken, 2015). In the past much attention has been paid to the accurate CFD modeling of the ABL, both using Reynolds-averaged Navier-Stokes and large-eddy simulation (LES) approaches.

LES (Sagaut, 2006), which is a high-fidelity approach for the unsteady simulation of turbulent flows, has been successfully applied to simulation of ABL (e.g., Andren et al., 1994; Beare et al., 2006; Nieuwstadt et al., 1993; P. Siebesma et al., 2003). Among the key issues raised in the development of LES, one must mention the development of i) subgrid models to account for the influence of unresolved scales of motion

on the resolved ones, ii) wall models when the grid is too coarse to allow for the use of the no-slip boundary condition at solid walls, and iii) well-suited numerical schemes that ensure stable simulations without masking the physical subgrid model effects.

Most of numerical tools for simulation of ABL flows are developed in the framework of conventional finite difference or finite volume methods, for example, UCLA-LES (Stevens et al., 2005), PALM (Maronga et al., 2015), ICON (Dipankar et al., 2015), MicroHH (Heerwaarden et al., 2017), PyCLES (Pressel et al., 2015), and EULAG (Prusa et al., 2008). The lattice Boltzmann method (LBM) is an alternative approach for the simulation of complex fluid dynamic problems, which is a recast of the Navier-Stokes equations in a form of simplified kinetic equations for the time evolution of probability distribution function of designer particles. This numerical method is based on a two steps algorithm with first a local treatment called the collision step and then a streaming of the postcollision to the first-order neighbors of the local node. This procedure ensures advantages for massively parallel computations since there is no need to access second or third order neighbors as it is done for high order numerical scheme in classical Navier-Stokes methods. This method is classically discretized on Cartesian grids with hierarchical embedded sub domains using a ratio of two on the grid spacing between each sub domains and the use of immersed boundary conditions for boundary treatment. Using this procedure, the preprocessing step in case of complex area is much more easier than with classical methods. The LBM is also very interesting considering its low numerical dissipation for unsteady flows. In summary, the benefits of LBMs include strong scalability in high-performance computing, low numerical dissipation, and the ability to simulate extremely complex geometry. LBM can be regards as a mesh-free method, which can significantly reduce the turnaround time including meshing compared with conventional methods. Thanks to its advantages, the LB methods quickly extended to large scale and spread toward exascale applications: automatic shape optimization of full-scale vehicles (Cheylan et al., 2019), urban scale environment flows (Ahmad et al., 2017; Jacob & Sagaut, 2018), meteorological flows (Feng et al., 2019a), and complex biological flows (Chateau et al., 2017) have been successfully addressed, often with outstanding results.

LES has been implemented within the lattice Boltzmann framework using mainly the subgrid model (e.g., Bartlett et al., 2013; Eggels, 1996; Hou et al., 1994; Premnath et al., 2009a,b; Teixeira, 1998; Yu et al., 2006). In one approach, subgird modeling can be theoretically developed in the mesoscopic physics framework, which possesses some inherent consistency with kinetic theory and multiscale analysis (Chen et al., 2004; Succi, 2020). In the other approach, the existing subgrid modeling techniques in Navier-Stokes equations can be incorporated in the LB models, such as Smagorinsky model (Teixeira, 1998; Wilhelm et al., 2020), approximate deconvolution model (Malaspinas & Sagaut, 2011; Sagaut, 2010). Classically, the eddy viscosity approach in LBM is that subgrid scale dynamics can be parameterized via a turbulent or eddy viscosity that is added to the molecular viscosity giving a total viscosity to be used in the LBM algorithm. Several extensions have been proposed for compressible flows of low-speed thermal flows but, to the knowledge of the authors, a LBM-based LES approach for atmospheric flows including stratification/buoyancy effects, humidity, condensation effects and complex media such has forest canopy has not been proposed up to now.

This paper describes a lattice Boltzmann tool for LES of turbulent flows and thermal convection in ABLs, including neutral, stable, convective, and cloudy convective ABLs as well as urban flows. The paper is organized as follows. Section 2 reviews governing macroscopic equations along with condensation and subgrid model. Section 3 presents the LBM, the finite difference method for water transport, and wall model implementation in boundary conditions. Section 4 investigates and discusses simulations on neutral, stable and convective ABL with canopy effects, as well as cumulus convection with phase change. The LBM-LES tool is then assessed considering two urban flow configurations in Section. 5. Finally, Section 6 summarizes the capabilities and assessment of the present tool and draws perspectives.

2. Equations of Motion

The ABL is assumed to be a mixture of dry air, water vapor, and liquid water, with respective mass fractions q_d, q_v and q_l (q_v being often referred to as specific humidity). A well-known approximation in the study of atmospheric and oceanic flows is the so-called Boussinesq approximation, which basically assumes that

density variations due to buoyancy forces are small compared to a reference state. The reference state is taken to be a hydrostatic state (ρ_0, p_0, T_0). Commonly, hydrostatic pressure p_0 and T_0 decrease with height by

$$\frac{\mathrm{d}p_0}{\mathrm{d}z} = -\rho_0 g, \frac{\mathrm{d}T_0}{\mathrm{d}z} = -\frac{g}{c_p} \tag{1}$$

Instead, one often uses the potential temperature θ

$$\theta = T\left(\frac{p_0(0)}{p_0(z)}\right)^{R_\mathrm{d}/c_\mathrm{p}} \tag{2}$$

Since $\mathrm{d}\theta_0 = 0$ in the isentropic reference state, one finds that the reference potential temperature is constant, $\theta_0 = \Theta_0$.

2.1. Navier-Stokes Equations

The governing equations of turbulent flows in ABLs are the filtered Navier-Stokes equations under the Boussinesq approximation.

$$\frac{\partial u_i}{\partial x_i} = 0 \tag{3a}$$

$$\frac{\partial u_i}{\partial t} + \frac{\partial u_j u_i}{\partial x_j} = -\frac{1}{\rho_0}\frac{\partial p''}{\partial x_i} + \frac{\partial}{\partial x_j}\left(\nu\frac{\partial u_i}{\partial x_j} - \overline{u_i' u_j'}\right) + F_{b,i} + F_{c,i} \tag{3b}$$

where u_i denotes the components of the velocity vector (u_x, u_y, u_z) and x_i represents the components of the position vector (x, y, z). The hydrodynamic pressure $p'' = p - p_0(z)$ represents the departure of the pressure p from reference state pressure $p_0(z)$. $F_{b,i}$ is the buoyancy term due to the gravity. $F_{c,i}$ is the Coriolis term due to the Earth's rotation. The turbulent stress $\overline{u_i' u_j'}$ denotes the subgrid momentum flux, which is responsible for the complicated chaotic nonlinear nature of turbulent flows. Hereafter $''$ are deviations from the hydrostatic reference state and $'$ indicate fluctuations from the filtered value of the variable.

2.2. Temperature and Water

Associated prognostic conservation equations for the temperature liquid and vapor mass fractions are (the air mass fraction being deduced as $q_d = 1 - q_v - q_l$)

$$\frac{\partial \theta}{\partial t} + u_i\frac{\partial \theta}{\partial x_i} = \frac{\partial}{\partial x_i}\left(D_\theta\frac{\partial \theta}{\partial x_i} - \overline{\theta' u_i'}\right) + \frac{L_v\theta}{c_p T}\dot{Q} \tag{4a}$$

$$\frac{\partial q_v}{\partial t} + u_i\frac{\partial q_v}{\partial x_i} = \frac{\partial}{\partial x_i}\left(D_q\frac{\partial q_v}{\partial x_i} - \overline{q_v' u_i'}\right) - \dot{Q} \tag{4b}$$

$$\frac{\partial q_l}{\partial t} + u_i\frac{\partial q_l}{\partial x_i} = \frac{\partial}{\partial x_i}\left(D_q\frac{\partial q_l}{\partial x_i} - \overline{q_l' u_i'}\right) + \dot{Q} \tag{4c}$$

Here, c_p is the mass heat capacity of dry air; D_θ and D_q are the temperature and water diffusion coefficients. $\dot{Q}$ is the mass transfer rate between the liquid and gas water phases and L_v is the mass latent heat of water. $\overline{\theta' u_j'}$, $\overline{q_v' u_j'}$ and $\overline{q_l' u_j'}$ are subgrid fluxes of heat, vapor and liquid water fractions. The subgrid terms are closed in the next section using the eddy viscosity paradigm. The mass transfer rate between the liquid and gas water phases $\dot{Q}$ can be directly included into the conservation equations, thereby reducing the number of partial differential equations, and resulting in a condensation model based on two invariant variables

(mass fraction of total water q_t and liquid water potential temperature θ_l). The model based on a set of governing equations about invariant variables (q_t, θ_l) is referred to as the 1eq model, whereas the model based on the variables (q_l, q_v, θ) is referred to as the 2eq model. The 1eq model is detailed in Appendix A.

2.3. Phase Transition Modeling

It is assumed in the present model (see Sommeria, 1976 for details) that the rate of phase transition is infinitely fast, or equivalently, that the liquid and gas phases are in thermo-chemical equilibrium at every time. Under this assumption, saturation properties provide additional relations between q_v and q_l. The saturation specific humidity is

$$q_s = \frac{\epsilon e_s}{p_0(z) - (1-\epsilon)e_s}, \tag{5}$$

in which the saturation pressure of water vapor can be approximated as

$$e_s = 610.78 \exp\left[17.269 \frac{T - 273.16}{T - 35.86}\right]. \tag{6}$$

and where $\epsilon = R_d/R_v$ is the molecular mass ratio of vapor water to that of dry air.

Under the infinitely fast relaxation approximation, the source term in Equation 4 is given by $\dot{Q} = \Delta q_l \,/\, \Delta t$. In practical numerical implementation, Δq_l is straightforwardly used, which can then be computed from

$$\Delta q_l = \begin{cases} -q_l & \text{if } q_v < q_s \text{ and } q_l < \Delta q_l \\ (q_v - q_s) \,/\, \alpha & \text{otherwise} \end{cases} \tag{7}$$

with (Sommeria, 1976)

$$\alpha = 1 + \frac{\epsilon q_s L_v^2}{c_p R_d T_0^2}\left(\frac{\theta_0^2}{\theta^2} - \frac{\theta_0}{\theta}\frac{R_v T_0}{L_v}\right). \tag{8}$$

The virtual temperature θ_v in the buoyancy term is defined hereafter as

$$\theta_v = \theta\left[1 - \left(1 - \frac{1}{\epsilon}\right)q_v - q_l\right], \tag{9}$$

The mass fraction of liquid water and vapor water can be computed by the phase transition model of the 1eq model which is detailed in Appendix A. Thus, the potential temperature used in Equation 9 can be computed from liquid water and liquid water potential temperature by

$$\theta = \theta_l + \frac{L_v}{c_p\,\Pi} q_l. \tag{10}$$

2.4. Buoyancy and Coriolis Forces

The external force terms like the buoyancy term in Equation 3b are incorporated through a body force $F_i = F_{b,i} + F_{c,i}$. Under the Boussinesq approximation, the buoyancy term is given by,

$$F_{b,z} = \frac{g}{\Theta_0}\left(\theta_v - \Theta_0\right) \tag{11}$$

The effects of a rotating reference frame on an f plane can be included through the Coriolis force. The acceleration due to the Coriolis force $F_{f,i}$ is computed for the two horizontal velocity components as

$$F_{c,x} = -f(V_g - u_y) \tag{12}$$

$$F_{c,y} = f(U_g - u_x) \tag{13}$$

where U_g and V_g are the geostrophic wind components. A similar approach is used for all additional force terms considered in the present study, for example, canopy drag $F_{c,i}$ in Equation 3b. Specific components canopy drag are discussed in Section 4.5.

2.5. Subgrid Modeling

The governing equations of turbulent flows, thermal convection and humidity transport in ABLs are the filtered Navier-Stokes equations. The subgrid terms $\overline{u_i' u_j'}$, $\overline{\theta' u_j'}$, $\overline{q_v' u_j'}$ and $\overline{q_l' u_j'}$ are closed in the present work using the eddy viscosity paradigm. Therefore, the subgrid fluxes are expressed as

$$\overline{u_i' u_j'} = -\nu_t \left(\frac{\partial u_i}{\partial x_j} + \frac{\partial u_j}{\partial x_i} \right), \tag{14a}$$

$$\overline{\theta' u_j'} = -D_{h,t} \frac{\partial \theta}{\partial x_j}, \tag{14b}$$

$$\overline{q_v' u_j'} = -D_{q,t} \frac{\partial q_v}{\partial x_j}, \tag{14c}$$

$$\overline{q_l' u_j'} = -D_{q,t} \frac{\partial q_l}{\partial x_j} \tag{14d}$$

where ν_t, $D_{h,t}$, and $D_{q,t}$ are the subgrid viscosity, subgrid thermal diffusivity, and subgrid humidity diffusivity, respectively. In the classical Smagorinsky approach, the subgrid viscosity is given by,

$$\nu_t = \lambda^2 \mid S \mid \tag{15}$$

where $\lambda = (C_S \Delta)$ is a mixing length defined by the Smagorinsky constant C_S and a filter length Δ (taken equal to the grid size in this work) and $\mid S \mid = \sqrt{2 S_{ij} S_{ij}}$ is the magnitude of the strain rate tensor,

$$S_{ij} = \frac{1}{2} \left(\frac{\partial u_i}{\partial x_j} + \frac{\partial u_j}{\partial x_i} \right) \tag{16}$$

Since stratification has an effect on subgrid scales of motion and therefore the energy transfer from resolved to subgrid scales, the amplitude of subgrid viscosity must be modified accordingly. This is classically done by modifying the subgrid length scale (Deardorff, 1980; Moeng, 1984). In the case of stable stratification, the eddy viscosity $\nu_t = \lambda^2 f_B |S|$ is reduced by the buoyancy factor f_B.

$$f_B = \begin{cases} 1, & \text{for } N^2 \le 0 \\ \max\left[0, \sqrt{1 - \dfrac{N^2}{Pr_{t,h} \mid S \mid^2}} \right], & \text{for } N^2 > 0 \end{cases} \tag{17}$$

where $N^2 = g / \Theta_0 \times \partial \overline{\theta} / \partial z$. For subgrid heat flux in filtered temperature equation, the turbulent thermal diffusivity is related to eddy viscosity through a turbulent Prandtl number

$$Pr_{t,h} = \frac{\nu_t}{D_{h,t}} \tag{18}$$

In this study, the vapor and liquid water fractions are assumed to have the same humidity diffusivity. Following the same analogy, the humidity diffusivity is related to the thermal diffusivity by

$$Pr_{t,q} = \frac{\nu_t}{D_{q,t}} \tag{19}$$

where $D_{q,t}$ is turbulent humidity diffusivity and $Pr_{t,q}$ is turbulent Prandtl number for humidity. Hereafter, ν, D_θ and D_q denote the total viscosity, the total thermal diffusivity and the total humidity diffusivity, respectively. These total diffusivities include both molecular and turbulent parts.

2.6. Surface Layers and Boundary Conditions

2.6.1. Sponge Layers

It is worth noting that ABL simulations frequently use sponge zones to damp spurious wave generation at computational domain top boundary, and that an external force can also be used for that purpose. The damped solution field is expressed as,

$$\tilde{\phi}(t+\Delta t) = \phi(t+\Delta t) - \sigma_{\text{sponge}}(z)\left[\phi(t+\Delta t) - \phi_{\text{target}}\right] \tag{20}$$

where ϕ could be density, velocity, temperature, or humidity and ϕ_{target} its corresponding target value, and $\sigma_{sponge}(z)$ is the absorbing strength. The second term in the right hand of (20) correspond to the force to be added,

$$F_{s,i} = \sigma_{\text{sponge}}(z)\left(\phi(t+\Delta t) - \phi_{\text{target}}\right) \tag{21}$$

The shape of the absorbing strength and target values require some attention. Following (Xu & Sagaut, 2013), the following profile of absorbing strength is used in this work,

$$\sigma_{\text{sponge}}(z) = \frac{3125(L_{\text{sponge}} - z)(z - z_0)^4}{256(L_{\text{sponge}} - z_0)^5} \tag{22}$$

where L_{sponge} is the width of the sponge layer, and z_0 is its starting position. On the other hand, the target field ϕ_{target} is often given by the test case specification; if it is not known, it is set equal to an average field calculated at each time step using the method presented in (Chevillotte & Ricot, 2016), namely,

$$\bar{\phi}(t+\Delta t) = (1-C)\bar{\phi}(t) + C\phi(t+\Delta t) \tag{23}$$

where C is a small value parameter.

2.6.2. Surface Models

LES of ABL flows requires the use of wall models to account for small scale dynamics in the vicinity of the ground and additional effects such as roughness effects. Most of these models evaluate the surface fluxes of the horizontal momentum components, temperature and humidity using the Monin-Obukhov similarity theory. The Monin-Obukhov relationships for the bottom boundary are (Dyer, 1974),

$$\frac{\kappa z}{u_*}\frac{\partial u}{\partial z} = \phi_m(z/L) \tag{24a}$$

$$\frac{\kappa z}{\theta_*}\frac{\partial \theta}{\partial z} = \phi_h(z/L) \tag{24b}$$

$$\frac{\kappa z}{q_*}\frac{\partial q_t}{\partial z} = \phi_h(z/L) \tag{24c}$$

where $\kappa = 0.41$ is the Von Kármán constant, u_* is the friction velocity, θ_* is the characteristic temperature, q_* is the characteristic humidity, and L is the Obukhov length given by,

$$L = \frac{u_*^2 \theta_0}{\kappa g(\theta_* + 0.61\theta_0 q_*)} \tag{25}$$

The functions ϕ_m and ϕ_h depend on the stability parameter z/L which defines in turn the type of boundary layer. For neutral case $\phi_m = 1$ whereas ϕ_h does not apply because potential temperature is uniform over the domain. For other cases, these functions are given by (Dyer, 1974),

$$\text{if } z / L < 0 \qquad \phi_m = (1 - 16(z / L))^{-1/4} \tag{26a}$$

$$\phi_h = (1 - 16(z / L))^{-1/2} \tag{26b}$$

$$\text{if } z / L > 0 \qquad \phi_m = \phi_h = 1 + 5(z / L) \tag{26c}$$

where $z/L < 0$ for convective case, and $z/L > 0$ for stable case.

Besides, a surface model for turbulent viscosity is necessary to consider the fact that turbulence is damped close to the wall. A blending function is used at the second off-wall node considering the mixing length close to the wall

$$\frac{1}{\lambda^n} = \frac{1}{\lambda_0^n} + \frac{1}{(\kappa(z + z_0))^n} \tag{27}$$

where $\lambda_0 = C_S \Delta x$ and n is a free parameter, set to unity in the following simulations.

2.6.3. Boundary Conditions

In all simulations, a free slip condition is used for the top boundary, whereas the Monin-Obukhov wall model is implemented at the bottom boundary. The implementation of Monin-Obukhov formulation depends on the chosen boundary condition in the different stratification situations. Three possible options are available:

1. Both the friction velocity u_* and the characteristic dynamic temperature θ_* are specified when fixed momentum fluxes and a fixed surface heat flux are given. Under these conditions, the Obukhov length can be computed directly from expression (25). Thus, velocities, temperature, stress and heat flux of the first node from wall can be calculated according Monin-Obukhov formulation
2. The friction velocity u_* is given and surface heat flux is unknown. In this condition, L needs to be retrieved from the implicit relationship of Monin-Obukhov formulation. An iterative procedure is adopted to calculate L with fixed u_*. After L is obtained, L is used to obtain velocities, temperature, stress and heat flux in the same way with the first type
3. Both the friction velocity u_* and surface heat flux are unknown. In this condition, L needs to be retrieved from the implicit relationship of Monin-Obukhov formulation with two variables. A double loop iterative procedure is adopted to calculate L with variables u_* and θ_*
4. The treatment on humidity q_t and q_* is the same as the one of potential temperature. Then the vapor and liquid humidities q_v and q_l are calculated by phase transition model

3. Numerical Method: Hybrid Lattice Boltzmann Solver

3.1. The LBM

3.1.1. Basic Core

LBMs is developed from Lattice Gas Automata (Chen and Doolen, 1998; D'humières & Lallemand, 1986; Qian et al., 1992) for fluid dynamics. Space and time are classically discretized on a Cartesian grid, whereas

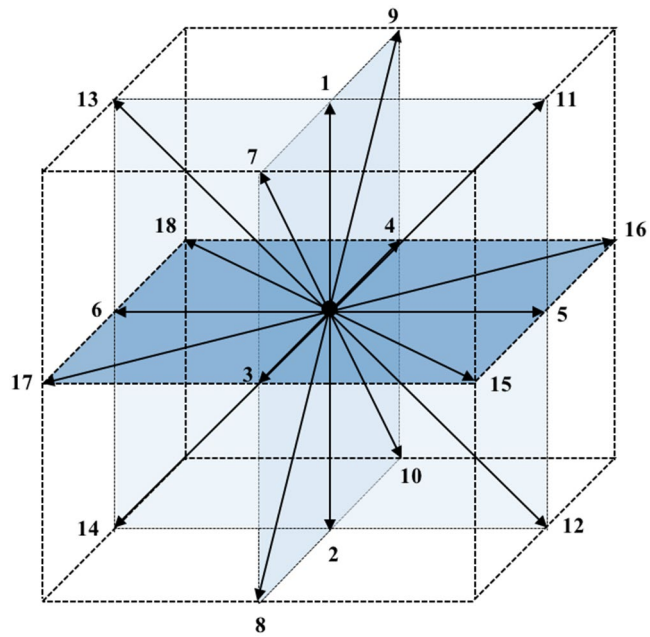

Figure 1. D3Q19 lattice.

particle velocities are discretized on a so-called DdQq lattice (d dimensions and q discrete velocities $c_{i\alpha}$). In this study the D3Q19 lattice stencils (Figure 1) is selected considering its lower number of degree of freedom compared with the D3Q27. The discrete velocities and corresponding weights are given as follows:

$$[c_{\alpha,i}, w_\alpha] = \begin{cases} [(0,0,0), 1/3] & \alpha = 0 \\ [(\pm1,0,0),(0,\pm1,0),(0,0,\pm1), 1/18] & \alpha = 1-6 \\ [(\pm1,\pm1,0),(\pm1,0,\pm1),(0,\pm1,\pm1), 1/36] & \alpha = 7-18 \end{cases} \tag{28}$$

The flow problem is then solved for $f_\alpha(x_i, t)$, namely the density distribution functions of particles with velocity $c_{\alpha,i}$ at (x_i, t) by the so-called lattice Boltzmann equation. Solution of this equation is usually computed using a second-order accurate Strang splitting, resulting in the definition of a local collision step (Equation 29a) followed by a nonlocal streaming step (Equation 29b) solved according a Lagrangian scheme:

$$f_\alpha^{\text{coll}}(x_i,t) = f_\alpha(x_i,t) + \Omega_\alpha, \tag{29a}$$

$$f_\alpha(x_i,t+\Delta t) = f_\alpha^{\text{coll}}(x_i - \Delta t c_{\alpha,i}, t) \tag{29b}$$

with Ω_α the collision operator and $f_\alpha^{\text{coll}}(x_i,t)$ the post collision distribution functions.

The schematic diagram of algorithm of LBM with collision and streaming steps are illustrated in Figure 2. In one time marching loop, the density distribution of particles marked in red advected from the nearest neighbor sites and then collided locally. Following the evolution of distribution functions, the macroscopic quantities such as density ρ and momentum ρu_i at the time step $t + \Delta t$ are updated by distribution functions in their velocity moments,

$$\rho = \sum_\alpha f_\alpha \tag{30a}$$

$$\rho u_i = \sum_\alpha f_\alpha c_{\alpha,i} \tag{30b}$$

For the local collision step, the single relaxation time model (BGK model) (Qian et al., 1992) is widely used in the literature because of its simplicity; however, it suffers from numerical instability in

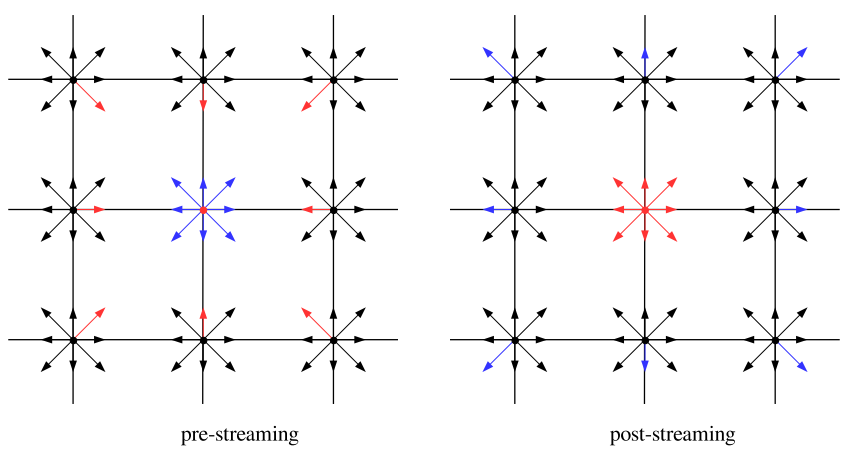

Figure 2. Schematic diagram of algorithm, left: prestreaming, right: poststreaming.

case of high Reynolds number flows (d'Humières et al., 2002). To solve this problem several collision models exhibiting better stability and accuracy properties have been developed last years such as multi relaxation times (d'Humières et al., 2002), cascaded (Geier et al., 2006; Geier, 2008), central moments (Premnath & Banerjee, 2011) or regularized models (Coreixas et al., 2017; Latt & Chopard, 2006; Malaspinas, 2015; Mattila et al., 2017). This approach was further improved by Jacob et al. (2018), who proposed a dynamic hybrid recursive regularized (HRR) single relaxation time model with self-adaptive dissipation for LES of high Reynolds number flows and Reynolds-Averaged Numerical Simulation (Wilhelm et al., 2018). Therefore, the HRR collision model (Jacob et al., 2018) is used in the present work. Starting from the BGK collision model (Equation 31a) and the classical decomposition of the distribution function in an equilibrium and a nonequilibrium part ($f_\alpha = f_\alpha^{\mathrm{eq}} + f_\alpha^{\mathrm{neq}}$), the postcollision distribution function is expressed as

$$f_\alpha^{\mathrm{coll}}(\vec{x},t) = f_\alpha(\vec{x},t) - \frac{1}{\tau}(f_\alpha - f_\alpha^{\mathrm{eq}}) \tag{31a}$$

$$= f_\alpha^{\mathrm{eq}}(\vec{x},t) + \left(1 - \frac{1}{\tau}\right) f_\alpha^{\mathrm{neq}} \tag{31b}$$

$$\approx f_\alpha^{\mathrm{eq}}(\vec{x},t) + \left(1 - \frac{1}{\tau}\right) \mathcal{R}(f_\alpha^{\mathrm{neq}}) \tag{31c}$$

where f_α^{eq} and f_α^{neq} are the equilibrium and non equilibrium function, $\mathcal{R}(f_\alpha{}^{\mathrm{neq}})$ is hybrid recursive regularization on off-equilibrium distribution function. τ is the dimensionless relaxation time which is linked with kinetic viscosity by $\nu = (2\tau - 1)/6$. Subgrid viscosity is implemented in the LBM method by replacing the molecular viscosity by the effective viscosity $\nu_{eff} = \nu + \nu_t$ in this formula, leading to a consistent implementation (Malaspinas & Sagaut, 2012; Sagaut, 2010). The local equilibrium distribution f_α^{eq} is given by

$$\begin{aligned} f_\alpha^{eq} = w_\alpha \Bigg\{ & \rho + \frac{c_{\alpha,i}\rho u_i}{c_s^2} + \frac{\mathcal{H}_{\alpha,ij}\mathcal{A}_{ij}^{(0)}}{2c_s^4} + \frac{1}{6c_s^6} \\ & \Big[3(\mathcal{H}_{\alpha,xxy} + \mathcal{H}_{\alpha,yzz})(\mathcal{A}_{xxy}^{(0)} + \mathcal{A}_{yzz}^{(0)}) + (\mathcal{H}_{\alpha,xxy} - \mathcal{H}_{\alpha,yzz})(\mathcal{A}_{xxy}^{(0)} - \mathcal{A}_{yzz}^{(0)}) \\ & +3(\mathcal{H}_{\alpha,xzz} + \mathcal{H}_{\alpha,xyy})(\mathcal{A}^{(0)}{}_{xzz} + \mathcal{A}_{xyy}^{(0)}) + (\mathcal{H}_{\alpha xzz} - \mathcal{H}_{\alpha,xyy})(\mathcal{A}_{xzz}^{(0)} - \mathcal{A}_{xyy}^{(0)}) \\ & + 3(\mathcal{H}_{\alpha,yyz} + \mathcal{H}_{\alpha,xxz})(\mathcal{A}_{yyz}^{(0)} + \mathcal{A}_{xxz}^{(0)}) + (\mathcal{H}_{\alpha,yyz} - \mathcal{H}_{\alpha,xxz})(\mathcal{A}_{yyz}^{(0)} - \mathcal{A}_{xxz}^{(0)})\Big] \Bigg\} \end{aligned} \tag{32}$$

where the second-order Hermite polynomials $\mathcal{H}_{\alpha,ij} = c_{i,\alpha}c_{j,\alpha} - c_s^2\delta_{ij}$ and $\mathcal{H}_{\alpha,ijk} = c_{i,\alpha}c_{j,\alpha}c_{k,\alpha} - c_s^2[c_\alpha\delta]_{ijk}$ correspond to the second and third order Hermite polynomials with $c_s = \sqrt{1/3}$ being lattice sound speed, $[c_\alpha\delta]_{ijk} = c_{\alpha,i}\delta_{jk} + c_{\alpha,j}\delta_{ik} + c_{\alpha,k}\delta_{ij}$ and δ_{ij} is the classical Kronecker matrix. $\mathcal{A}_{ij}^{(0)} = \rho u_i u_j$ and $\mathcal{A}_{ijk}^{(0)} = \rho u_i u_j u_k$ are respectively the second and third order coefficient of Hermite polynomials.

As previously discussed, the classical BGK collision model considering only the unfiltered non equilibrium distribution function $f_\alpha^{\mathrm{neq}} = f_\alpha - f_\alpha^{\mathrm{eq}}$ is not stable for high Reynolds flows. A stabilization procedure based on the reconstruction of the non equilibrium part is done through an hybrid recursive regularization (HRR [Jacob et al., 2018]) considering the projection of f_α^{neq} on the Hermite polynomials basis ($\mathcal{A}_{ij}^{(1)}$) and its approximation by finite differences ($\mathcal{A}_{ij}^{(1,\mathrm{FD})}$) expressed as

$$\mathcal{A}_{ij}^{(1)} = \sum_i c_{\alpha,i}c_{\alpha,j}f_\alpha^{\mathrm{neq}} \tag{33a}$$

$$\mathcal{A}_{ij}^{(1,\mathrm{FD})} \approx -\Delta t\bar{\tau}\rho c_s^2\left[\frac{\partial u_j}{\partial x_i} + \frac{\partial u_i}{\partial x_j} - \frac{2}{3}\frac{\partial u_k}{\partial x_k}\delta_{ij}\right] \tag{33b}$$

The HRR operator is then expressed as

$$\begin{aligned}\mathcal{R}(f_\alpha{}^{\mathrm{neq}}) = w_\alpha \Bigg\{ & \frac{\mathcal{H}_{\alpha,ij}\mathcal{A}_{ij}^{(1,\mathrm{HRR})}}{2c_s^4} + \frac{1}{6c_s^6} \\ & \Big[3(\mathcal{H}_{\alpha,xxy} + \mathcal{H}_{\alpha,yzz})(\mathcal{A}_{xxy}^{(1,\mathrm{HRR})} + \mathcal{A}_{yzz}^{(1,\mathrm{HRR})}) + (\mathcal{H}_{\alpha,xxy} - \mathcal{H}_{\alpha,yzz})(\mathcal{A}_{xxy}^{(1,\mathrm{HRR})} - \mathcal{A}_{yzz}^{(1,\mathrm{HRR})}) \\ & + 3(\mathcal{H}_{\alpha,xzz} + \mathcal{H}_{\alpha,xyy})(\mathcal{A}_{xzz}^{(1,\mathrm{HRR})} + \mathcal{A}_{xyy}^{(1,\mathrm{HRR})}) + (\mathcal{H}_{\alpha,xzz} - \mathcal{H}_{\alpha,xyy})(\mathcal{A}_{xzz}^{(1,\mathrm{HRR})} - \mathcal{A}_{xyy}^{(1,\mathrm{HRR})}) \\ & + 3(\mathcal{H}_{\alpha,yyz} + \mathcal{H}_{\alpha,xxz})(\mathcal{A}_{yyz}^{(1,\mathrm{HRR})} + \mathcal{A}_{xxz}^{(1,\mathrm{HRR})}) + (\mathcal{H}_{\alpha,yyz} - \mathcal{H}_{\alpha,xxz})(\mathcal{A}_{yyz}^{(1,\mathrm{HRR})} - \mathcal{A}_{xxz}^{(1,\mathrm{HRR})})\Big]\Bigg\}\end{aligned} \tag{34}$$

where $\mathcal{A}_{ij}^{(1,\mathrm{HRR})} = \sigma\mathcal{A}_{ij}^{(1)} + (1-\sigma)\mathcal{A}_{ij}^{(1,\mathrm{FD})}$ is the hybrid regularized second-order off-equilibrium moment with $\sigma \in [0,1]$ an arbitrary weighting coefficient and $\mathcal{A}_{ijk}^{(1,\mathrm{HRR})} = u_i\mathcal{A}_{jk}^{(1,\mathrm{HRR})} + u_j\mathcal{A}_{ki}^{(1,\mathrm{HRR})} + u_k\mathcal{A}_{ij}^{(1,\mathrm{HRR})}$ is the third order off-equilibrium moment recursively reconstructed. The second-order isotropic central difference scheme is employed to compute the numerical gradient operator and a value of $\sigma = 0.99$ is adopted in this work.

3.1.2. Implementation of Buoyancy, Coriolis, and Sponge Forces

The external force terms like the buoyancy term in Equation 3b are incorporated through a body force F_α added to the right hand side of Equation 29. The HRR lattice Boltzmann equation with forcing term is expressed as (see Feng, Boivin, et al., 2019)

$$f_\alpha^{\mathrm{coll}}(x_i,t) = f_\alpha^{\mathrm{eq}}(x_i,t) + \left(1 - \frac{1}{\tau}\right)\mathcal{R}(f_\alpha^{\mathrm{neq}}) + F_\alpha \tag{35}$$

and the macroscopic density ρ and momentum ρu_i incorporated the general forcing term F_i are updated as

$$\rho = \sum_\alpha f_\alpha \tag{36a}$$

$$\rho u_i = \sum_\alpha c_{\alpha,i} f_\alpha + \frac{\Delta t}{2} F_i \tag{36b}$$

where F_i are the components of the external force and the forcing term in HRR-LB equation is expressed as

$$F_\alpha = \left(1 - \frac{1}{2\tau}\right)\omega_\alpha \left[\frac{c_{\alpha,i} - u_i}{c_s^2} + \frac{c_{\alpha,j}u_j}{c_s^4}c_{\alpha,i}\right]F_i \tag{37}$$

3.1.3. Implementation of Boundary Conditions

In contrast to the conventional CFD methods, an extra step is required for implementation of the boundary condition in the LB method. By using the updated velocities on boundary nodes, the distribution functions on the first off-boundary nodes is recovered via the nonequilibrium reconstruction as follows

$$f_\alpha = f_\alpha^{\mathrm{eq}}(\rho,u_i) + f_\alpha^{\mathrm{neq}}(\mathcal{A}_{ij}^{(1)},\mathcal{A}_{ijk}^{(1)}). \tag{38}$$

where the density at the first off-boundary node is extrapolated from neighboring nodes. $\mathcal{A}_{ij}^{(1)}$ and $\mathcal{A}_{ijk}^{(1)}$ are computed as

$$\mathcal{A}_{ij}^{(1)} \approx -\Delta t\bar{\tau}\rho c_s^2\left[\frac{\partial u_j}{\partial x_i} + \frac{\partial u_i}{\partial x_j} - \frac{2}{3}\frac{\partial u_k}{\partial x_k}\delta_{ij}\right] \tag{39}$$

$$\mathcal{A}_{ijk}^{(1)} = u_i\mathcal{A}_{jk}^{(1)} + u_j\mathcal{A}_{ki}^{(1)} + u_k\mathcal{A}_{ij}^{(1)} \tag{40}$$

where the velocity gradients on boundary nodes are computed on these nodes using a first-order biased finite difference scheme, for example,

$$\left.\frac{\partial u_y}{\partial x}\right|_b = \frac{1}{\Delta x}(u_{y,b} - u_{y,i}) \tag{41}$$

where $u_{y,b}$ is the y component of velocity at boundary.

3.2. Finite Volume Method for Advected Scalar Quantities

For scalar fields like the total water specific humidity it is possible to use either another set of distribution functions (Zhang et al., 2011) or a hybrid approach in which conservation equations for these quantities are solved using a classical finite volume/finite difference method. The hybrid approach is used here, in order to minimize the number of degrees of freedom per cell of the global method.

The same method is used for all advected scalar quantities (temperature, humidities, etc.) The convective flux is constructed using the Monotonic Upstream-centered Scheme for Conservation Laws (MUSCL) scheme, while the classical second-order accurate centered difference scheme is adopted for the diffusion term and term of viscous dissipation. The third order MUSCL scheme (Kim et al., 2001) is adopted in this study to preclude spurious wiggles. For example, the x component of the advection term in Equation 4a is expressed as

$$u_x \frac{\partial \theta}{\partial x} = u_{x,i} \frac{\theta_{i+1/2} - \theta_{i-1/2}}{\Delta x} \tag{42}$$

$\theta_{i+1/2}$ for instance, can be given as

$$\theta_{i+\frac{1}{2}} = \begin{cases} \theta^L_{i+\frac{1}{2}}, u_i > 0 \\ \theta^R_{i+\frac{1}{2}}, u_i \le 0 \end{cases} \tag{43}$$

and

$$\begin{aligned} \theta^L_{i+\frac{1}{2}} &= \theta_i + \frac{\varphi(r_i)}{4}\left[(1-\kappa)\delta\theta_{i-\frac{1}{2}} + (1+\kappa)\delta\theta_{i+\frac{1}{2}}\right], \\ \theta^R_{i+\frac{1}{2}} &= \theta_{i+1} - \frac{\varphi(r_{i+1})}{4}\left[(1-\kappa)\delta\theta_{i+\frac{3}{2}} + (1+\kappa)\delta\theta_{i+\frac{1}{2}}\right], \end{aligned} \tag{44}$$

where $\kappa = 1/3$, and,

$$\begin{aligned} \delta\theta_{i+\frac{1}{2}} &= \left(\theta_{i+1} - \theta_i\right), \delta\theta_{i-\frac{1}{2}} = \left(\theta_i - \theta_{i-1}\right), \\ \delta\theta_{i+\frac{3}{2}} &= \left(\theta_{i+2} - \theta_{i+1}\right), \delta\theta_{i-\frac{3}{2}} = \left(\theta_{i-1} - \theta_{i-2}\right), \\ r_i &= \frac{\theta_i - \theta_{i-1}}{\theta_{i+1} - \theta_i} \end{aligned} \tag{45}$$

where i represents index of grid rather than lattice discrete velocity. The van Albada limiter function $\varphi(r) = 2r/(1 + r^2)$ is used to avoid spurious oscillations (Hirsch, 2007).

Besides, the diffusion term is approximated by calculating gradient by a central difference scheme.

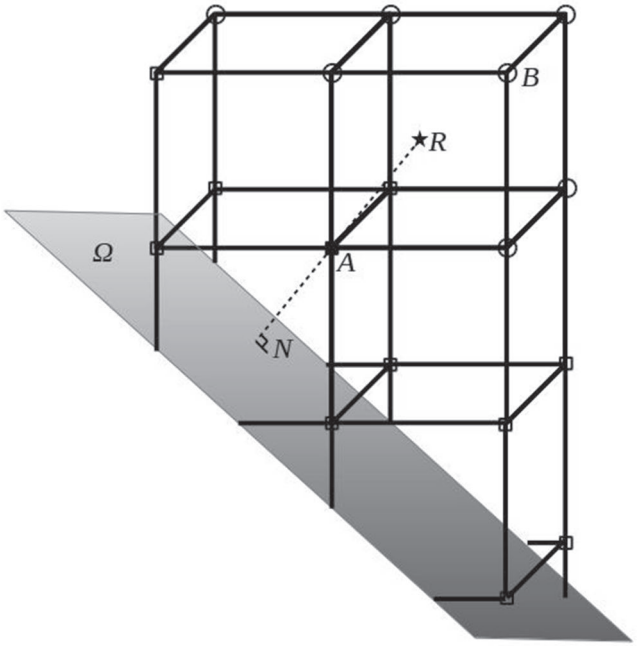

Figure 3. Immersed solid boundary in three-dimension.

$$\frac{\partial}{\partial x}(D_\theta \frac{\partial}{\partial x}\theta) = \frac{1}{\Delta x}\left[D_{\theta,i+1/2}\frac{\theta_{i+1}-\theta_i}{\Delta x} - D_{\theta,i-1/2}\frac{\theta_i-\theta_{i-1}}{\Delta x}\right],$$
$$D_{\theta,i+1/2} = \frac{1}{2}(D_{\theta,i}+D_{\theta,i+1}),\ D_{\theta,i-1/2} = \frac{1}{2}(D_{\theta,i}+D_{\theta,i-1}) \tag{46}$$

where D_θ is total diffusivity of potential temperature and the same expressions are used to solve for y and z directions.

3.3. Immersed Boundary Approach for Complex Geometries

The present LBM-LES tool is augmented via implementation of immersed boundary approach to handle arbitrary geometries while using embedded Cartesian grid. The previous boundary conditions for solid surfaces are implemented in a local reference frame associated to the solid surface in the following way.

Typically, the variables on boundary node A that will enforce a Dirichlet boundary condition for the wall model has to be computed. First, two references points (N and R) are defined and arranged, which are located on the normal line to the wall passing through the boundary node A as described in Figure 3. N is the intersection point of immersed solid surface Ω and the normal line. R is the reference point with $\overline{NR} = 2.5\Delta x$ distance away from point N. The macroscopic values on point R are interpolated from the neighbors of $\circ$ by using the Shepard's Inverse Distance Weighting (IDW) method (Shepard, 1968).

$$\phi(x_i) = \sum_{j=1}^{N}\frac{d(x_i,x_j)^{-p}}{\sum_{j=1}^{N} d(x_i,x_j)^{-p}}\phi(x_j), \tag{47}$$

$$d(x_i,x_j) = \sqrt{(x_j-x_i)^2+(y_j-y_i)^2+(z_j-z_i)^2} \tag{48}$$

where $d\ (x_i, x_j)$ denotes the distance between point x_i and its neighbor x_j. The exponent index p is a free parameter in the IDW method and $p = 2$ is typically recommended (Gao et al., 2007) and adopted in the present implementation. Once the variables of reference point R are computed, the wall models can be implemented in the local reference frame. Details of implementation of boundary conditions, including the coupling with wall models for turbulent flows, are available in (Feng et al., 2019b; Wilhelm et al., 2018).

4. Benchmarking: HRRLB-LES Solver for ABLs

4.1. Neutral Boundary Layer

ABL under neural condition proposed in the cross-comparisons of (Andren et al., 1994) with slight modifications is used to accessed the LBM-LES solver. We use here a simulation domain of 1,280 × 1,280 × 1,500 m as in (Chow et al., 2005). Periodic conditions are employed in the horizontal direction, and the roughness length for Monin-Obukhov similarity is set as $z_0 = 0.1$ m. The atmospheric boundary flow is driven by a large-scale pressure gradient which results from the balance with a geostrophic wind of $(U_g, V_g) = (10, 0)$ m s^{-1}. The following force is introduced through a source term in the lattice Boltzmann equation (see Equation 37),

$$F_{c,x} = -f(V_g - u_y) \tag{49a}$$

$$F_{c,y} = f(U_g - u_x) \tag{49b}$$

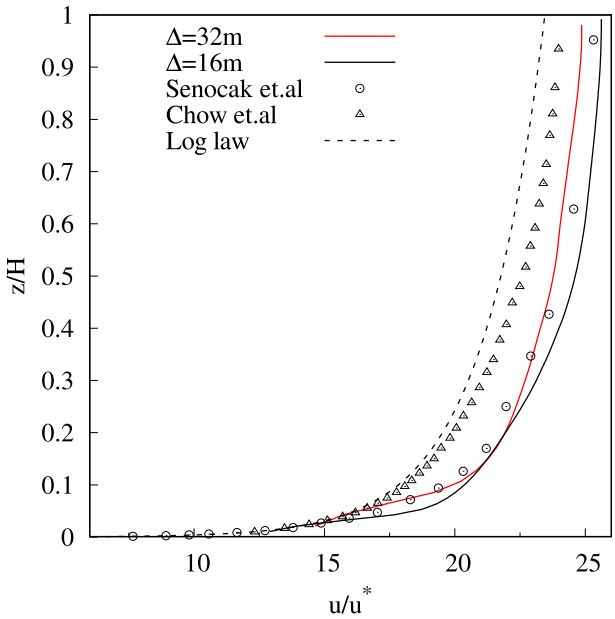

Figure 4. Mean velocity profile (neutral case).

where the Coriolis parameter is $f = 10^{-4}\ \mathrm{s}^{-1}$. Simulation was initialized with a reference density of $\rho_0 = 1\ \mathrm{kg\ m}^{-3}$, and the analytical Ekman profile for velocity given by (Cushman-Roisin & Beckers, 2009)

$$u_x = U_g\left(1 - \exp(-z\ /\ H)\cos(z\ /\ H)\right) \tag{50a}$$

$$u_y = U_g \exp(-z\ /\ H)\sin(z\ /\ H) \tag{50b}$$

where H is the domain height which corresponds approximately to the boundary layer height. The numerical simulation was performed over 30 dimensionless time periods tf as in (Chow et al., 2005). Two different grids were used with $\Delta x = 32$ m, $\Delta x = 16$ m, and average results were taken over the last six periods that correspond approximately to the inertial oscillation period $2\pi/f$.

Figure 4 shows the mean velocity profile compared with the results of (Senocak et al., 2007). The mean velocity is averaged in the horizontal plane direction and in time period, and it is normalized with u_*. The numerical results of finer mesh have a better agreement with the reference values. On the whole, it can be observed that even though grid is coarse, the LBM with Smagorinsky model can well predict the flow structures.

The friction velocity is crucial in prediction of fluid flow in ABL. Table 1 compares the values of friction velocity obtained in this work with those from the intercomparison (Andren et al., 1994). Quantitatively speaking, quite consistent results on difference grid resolutions are obtained by our LBM-LES solver. From the above observation, accuracy and compatibility of the wall model for neutral boundary layer is well proven in our simulations.

To obtain a more intuitive comparison, the normalized stresses obtained from time statistic of the neutral atmospheric boundary layer are compared with reference values is plotted in Figure 5. With the increasing grid resolution, the results gradually close to total stress in reference, which implies the good grid convergence feature of the present LBM-LES solver.

4.2. Stable Boundary Layer

The stable atmospheric boundary layer (SBL) is considered the most challenging case for LES because eddies are smaller than in the neutral case; therefore, the resolved turbulence is harder to maintain if the grid is not fine enough. Here we simulate the SBL proposed in the intercomparison of (Beare et al., 2006). It consists of a 400 × 400 × 400 m domain where the flow is driven by a geostrophic wind of $U_g = 8\ \mathrm{m\ s}^{-1}$, $V_g = 0\ \mathrm{m\ s}^{-1}$ and Coriolis parameter of $f = 1.39 \times 10^{-4}\ \mathrm{s}^{-1}$. Periodic boundary conditions are applied in the horizontal directions. At the top boundary, a free slip condition is applied along with a sponge layer over the last 100 m. Monin-Obukhov relationships with a roughness length of $z_0 = 0.1$ m and a surface cooling of 0.25 K h^{-1} are applied to the bottom boundary.

Table 1
Friction Velocity (Neutral Case)

	u_* (m/s)
$\Delta x = 16$m (Smag)	0.419
$\Delta x = 32$m (Smag)	0.429
Andren/Moeng	0.425
Mason/Brown bsct	0.448
Mason/Brown nbsct	0.402
Nieuwstadt	0.402
Schumann/Graf	0.425

The initial velocity profile is a constant velocity in the horizontal direction equal to the geostrophic values $u_x = U_g$, $u_y = V_g$ and zero vertical velocity. The initial temperature profile is set as,

$$\theta = \begin{cases} 265\ \mathrm{K} & z \le 100\ \mathrm{m} \\ 265 + \left(z - 100\right)\Gamma\ \mathrm{K} & z > 100\ \mathrm{m} \end{cases} \tag{51}$$

where $\Gamma = 0.01\ \mathrm{K\ m}^{-1}$ is a constant slope of potential temperature from height of 100 m to the top of the domain. Initially, a random perturbation of 0.1 K is applied below 50 m is to trigger the turbulence flow.

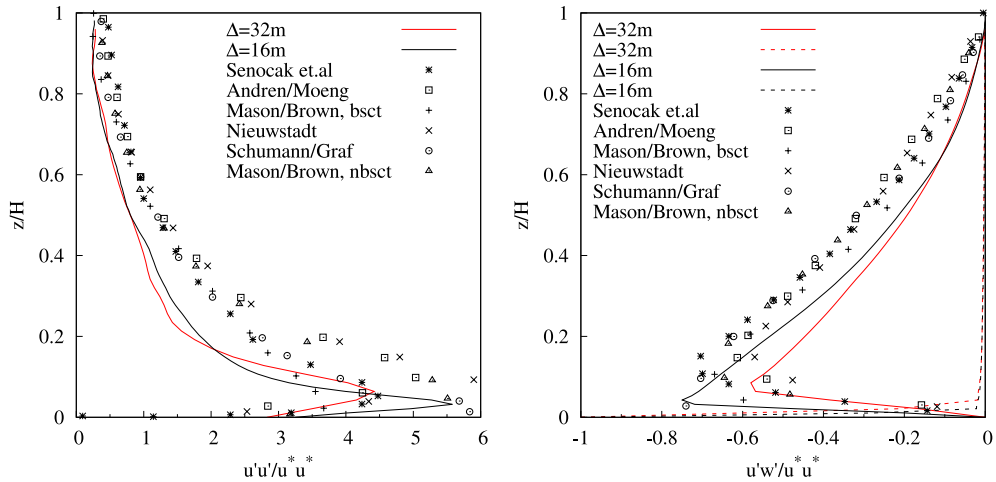

Figure 5. Momentum flux (neutral case). For component $u'w'$, the resolved part is denoted by the solid line and the modeled on is plotted by the dash line.

Simulations were performed using 3.125, 6.25, and 12.5 m grids with subgrid model. Smagorinsky constant of $C_S = 0.23$ for subgrid model was suggested in (Beare et al., 2006) by sensitivity analysis is too large for the 6.25 m resolution in our study, thus it is set to $C_S = 0.15$ and used the same value for the 3.125 and 12.5 m grids.

The numerical simulation time was set as 9 h, and results were averaged over the last hour. Figure 6 shows mean profiles of velocity and potential temperature compared to the results with 2.0 m mesh in the intercomparison (Heerwaarden et al., 2017). Results by the present LBM-LES solver well reproduced the supergeostrophic jet characteristic of stable layers. Temperature profile on Figure 6 have a good agreement with references values at the bottom of the boundary layer, and the inversion layer takes place at a little higher altitude.

4.3. Convective Boundary Layer

The convective boundary layer case is taken from (Nieuwstadt et al., 1993) who conducted an intercomparison of large-eddy codes from four research groups. The simulation domain is 6,400 × 6,400 × 2,400 m to which we add a sponge layer of 600 m, so the total domain height in our study is 3,000 m. The roughness length used for the Monin-Obukhov relationships is $z_0 = 0.16$ m.

The convective boundary layer is set in terms of temperature and convective velocity scales defined by,

$$w_* = \left(\frac{g}{T_0} Q_s z_i\right)^{1/3}, T_* = \frac{Q_s}{w_*} \tag{52}$$

where g is the gravity, T_0 is a reference temperature, Q_s is the surface temperature flux, and z_i is the boundary layer height. As the boundary height is not known a priori, an approximate boundary height of $z_{i0} = 1{,}600$ m is used to define initial conditions. The surface is heated by a constant temperature flux of $Q_s = 0.06$ K m s^{-1}. Considering Q_s, z_{i0}, and a reference temperature $T_0 = 300$ K, the convective velocity and temperature scales are $w_{*0} = 1.46$ m s^{-1} and $T_{*0} = 0.041$ K. A time scale derived from z_{i0} and w_{*0} is $t_{*0} = 1{,}096$ s. With these scalings, the initial conditions are given by,

For $z \le z_{i1} = 0.844 z_{i0}$

$$\theta = T_0 + 0.1r\left(1 - \frac{z}{z_{i1}}\right) T_{*0} \tag{53a}$$

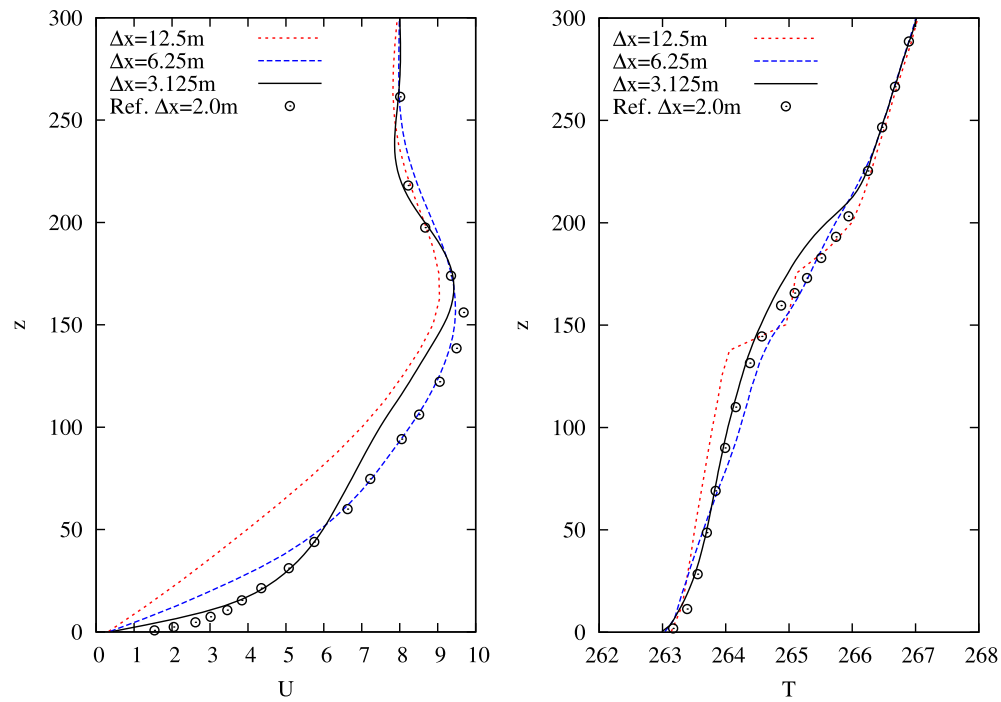

Figure 6. Mean velocity and temperature (stable case). The results were averaged on the ninth hour and compared with the reference data in (Heerwaarden et al., 2017).

$$u_z = 0.1r\left(1 - \frac{z}{z_{i1}}\right)w_{*0} \tag{53b}$$

$$u_x = u_y = 0 \tag{53c}$$

For $z > z_{i1}$

$$\theta = T_0 + \left(z - z_{i1}\right)\Gamma \tag{54a}$$

$$u_x = u_y = u_z = 0 \tag{54b}$$

where r is a random number uniformly distributed between −0.5 and 0.5, and $\Gamma = 0.003$ K m^{-1} is a constant temperature gradient over the boundary layer. Simulations were performed for 11 time periods $11t_*$, and averaged results are calculated on the last 1 h.

The research groups that participated in the intercomparison of (Nieuwstadt et al., 1993) used different parameters for discretization and subgrid model. Some of them used non uniform grids, so their vertical meshes ranges from 20 m to 60 m. Two of the groups reported a Smagorinsky constant of $C_S = 0.18$ and turbulent Prandtl of $Pr = 0.33$ even though subgrid model differs among them. We decided to use these values in our simulations, and a uniform mesh with two resolutions of $\Delta x = 50$ m and $\Delta x = 25$ m.

The average temperature profile by our LBM-LES solver is plotted in Figure 7. We compare here our results with that from (Schmidt & Schumann, 1989) where averages are taken at $6t_*$, since the temperature profiles were not given in (Nieuwstadt et al., 1993). A common characteristic of the convective boundary layer is that mean temperature is roughly constant in the mixed layer, approximately the zone between 0.1 and 0.9 z/z_{i0}. This characteristic is well satisfied with the $\Delta x = 25$ m and $\Delta x = 50$ m mesh sizes.

Figure 7 also shows the profile of vertical turbulent heat flux. The boundary layer height is defined as the height where this flux reaches its minimum value; this minimum value is known as the entainment flux

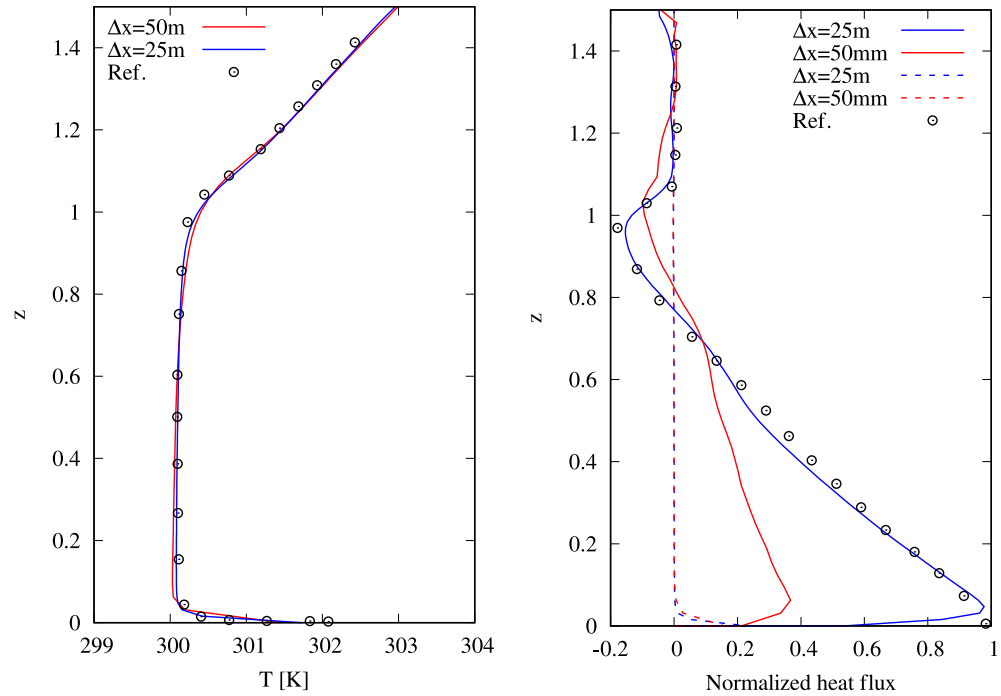

Figure 7. Mean temperature at $6t_*$ and resolved vertical heat flux at $6.5t_*$ (convective case). For normalized heat flux, the resolved part is denoted by the solid line and the modeled on is plotted by the dash line.

$-\langle w'\theta'\rangle$. In general, our simulations at coarse grid give smaller values for the entrainment flux in (Nieuwstadt et al., 1993). The main reason is the under-resolution of small scale turbulent motion on coarse grid, which is not balanced by a posteriori reconstruction of subgrid contributions. As discussed in Chapter 9 of (Sagaut, 2006), reconstruction of subgrid fluxes is a controversial issue since LES filter is unknown and subgrid viscosity model are not designed to model the subgrid fluxes but to enforce a physical balance of resolved kinetic energy.

4.4. Shallow Cumulus Convection

A shallow cumulus convection is simulated by the LBM-LES solver to evaluate the moist thermodynamics and its interaction with subgrid modeling. The shallow cumulus convection simulations follows the setup of the Barbados Oceanographic and Meteorological Experiment (BOMEX) model intercomparison case (P. Siebesma et al., 2003). This is the most prevalent shallow cumulus LES case. Siebesma and Cuijpers (Siebesma and Cuijpers, 1995) conducted an early LES based on a case from the BOMEX field experiment.

In this case, a height dependent geographic wind u_g is given by a linear formula $u_g = (-10 + 1.8 \times 10^{-3} z)$ m s^{-1} and the Coriolis parameter is set to $f = 0.376 \times 10^{-4}$s^{-1}. The initial conditions for velocity, liquid water potential temperature and total water mixing ratio are linear profiles following the values given on Table 2.

The temperature and humidity surface fluxes are 8×10^{-3} K m s^{-1} and 5.2×10^{-5} m s^{-1}, respectively. The shear stresses are prescribed by $\overline{u_i w} = -u_*^2 u_i \,/\, (u_1^2 + u_2^2)^{1/2}$, with $u_* = 0.28$ m s^{-1}.

Moreover, additional terms are added to represent the large-scale forcing which could not be represented directly in the LES. The source terms of momentum conservation equations, temperature equation, and water equations are parameterized considering the effects of large-scale subsidence, radiative cooling and moisture effects. Their details are described in (P. Siebesma et al., 2003).

The LBM-LES solver with condensation scheme has been employed to reproduce the case at two resolutions of $\Delta x = 80$ m and 40 m in domain of $5{,}000 \times 5{,}000 \times 3{,}000$ m. Time interval is 0.54 s on coarse mesh and

Table 2
Initial Conditions for Cumulus Case

Height (m)	q_t (g kg^{-1})	θ_l (K)	u (m s^{-1})	v (m s^{-1})
0	17.0	298.7	−8.75	0
520	16.3	298.7		
700			−8.75	
1,480	10.7	302.4		
2,000	4.2	308.2		
3,000	3.0	311.85	−4.61	0

0.27 s on fine mesh, respectively. Smagorinsky constant of $C_S = 0.23$ and turbulent Prandtl of $Pr = 0.33$ is adopted both for potential temperature and water equations. Small random perturbations are applied to initiate turbulence, and both of the simulations are run for 6 hours. Statistics are performed during the final hour.

Figure 8 shows profiles of turbulence statistics from the simulations. All of the results are in good agreement with the reference data from (P. Siebesma et al., 2003). Consistent results are clearly obtained with comparison of data from coarse mesh and fine mesh. The mean profiles of velocities, potential temperature, vapor water and liquid water on fine mesh are confirmed closely to reference values. The mixed region below the surface of 540 m is well captured, which has valid the accuracy of wall model with complex moist thermophysics. Furthermore, the conditionally unstable layer from 540 m to 1,500 m, and the inversion layer from 1,500 to 2,000 m are also clearly observed in the results. Both the results obtained by 1eq model and 2eq model are presented in Figure 8 and the 1eq model (liquid water potential temperature θ_l and total water q_t) exhibited better performance on prediction of liquid water and liquid water potential temperature, thus the 1eq model is used as the default condensation model in the ProLB solver.

4.5. Neutral, Stable, and Convective ABL With Canopy Effects

The present LBM-LES method is further assessed considering the flows in neutral, stable and convective boundary layer over a forest canopy. In this configuration, the forest is modeled as a nonuniform homogenized porous medium. The forest model is implemented as a volumetric source term in both the macroscopic momentum and temperature equations. More precisely, altitude-dependent drag force and heat release source term are introduced within the forest. This heat source is assumed to be proportional to solar radiation; therefore, it achieves the largest value at the canopy top and diminishes exponentially through it with an extinction coefficient $\gamma = 0.6$,

$$S_\theta = \frac{\partial}{\partial z}\left(Q_h \exp(-\gamma A_c)\right) \tag{55}$$

The canopy-top heat flux Q_h is prescribed as a constant value that defines the type of stability, namely a positive source for convective case, a negative source for stable case, and no source for the neutral case. The values studied in this section are, 1) Neutral BL: $Q_h = 0.0$ K m s^{-1}, 2) Convective BL: $Q_h = 0.015$ K m s^{-1}, and 3) Stable BL: $Q_h = -0.0035$ K m s^{-1}. The downward cumulative leaf-area index A_c in Equation 55 is given by,

$$A_c = \int_z^h a_f dz \tag{56}$$

The leaf-area density a_f is related to the forest profile. Nebenführ and Davidson (2015) used an empirical profile, while a beta probability distribution profile is used by (Markkanen et al., 2003). The later solution is used in the present work, with parameters $\alpha = 3$ and $\beta = 2$ as in (Banerjee et al., 2017), leading to

$$a_f\left(\frac{z}{h}\right) = \frac{\left(\frac{z}{h}\right)^2\left(1-\frac{z}{h}\right)}{\int_0^1\left(\frac{z}{h}\right)^2\left(1-\frac{z}{h}\right)d\left(\frac{z}{h}\right)} \tag{57}$$

Note that this is a dimensionless expression, which can be adapted to different forest parameters. Thus, using the same leaf-area index LAI = 4.3 as (Nebenführ & Davidson, 2015), the dimensional value of leaf-area density is obtained through $a_f(z) = (LAI/h)a_f(z/h)$.

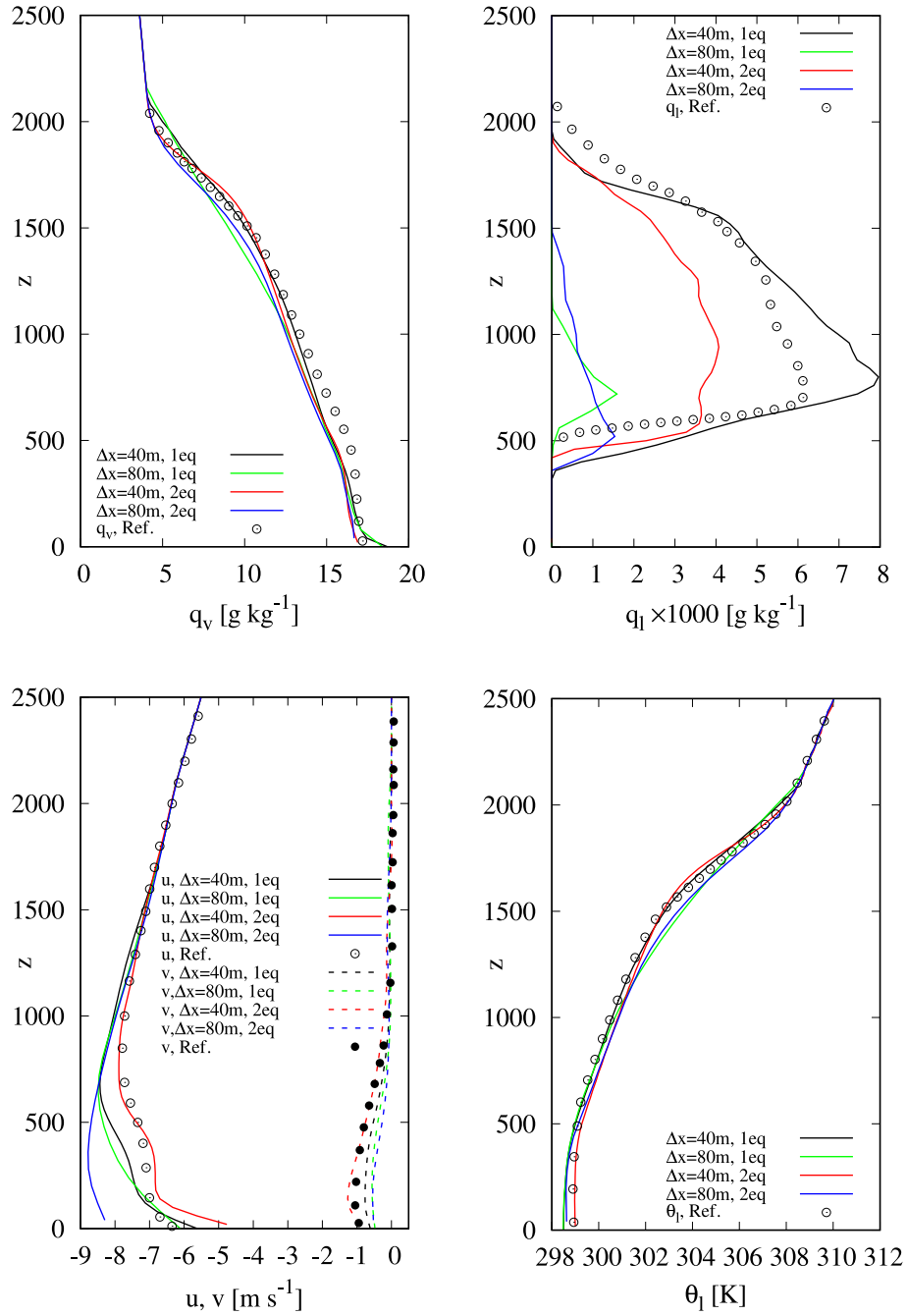

Figure 8. Mean profiles (convective cumulus case).

The forest is assumed to be horizontally homogeneous with a drag coefficient of $C_D = 0.15$. The drag force is finally evaluated as

$$F_{f,i} = -C_D a_f(z) U u_i \tag{58}$$

Results are compared with the Navier-Stokes based reference LES simulations and field measurements from a forested region in the south-east of Sweden reported in (Nebenführ & Davidson, 2015). The computational domain size is 400 × 400 × 400 m with a canopy of height $h = 20$ m. The flow is driven by a geostrophic wind such as $U_g = 5$ m s^{-1}, $V_g = 0$ m s^{-1}, and the Coriolis parameter is set equal to $f = 1.22 \times 10^{-4}$ s^{-1}. The

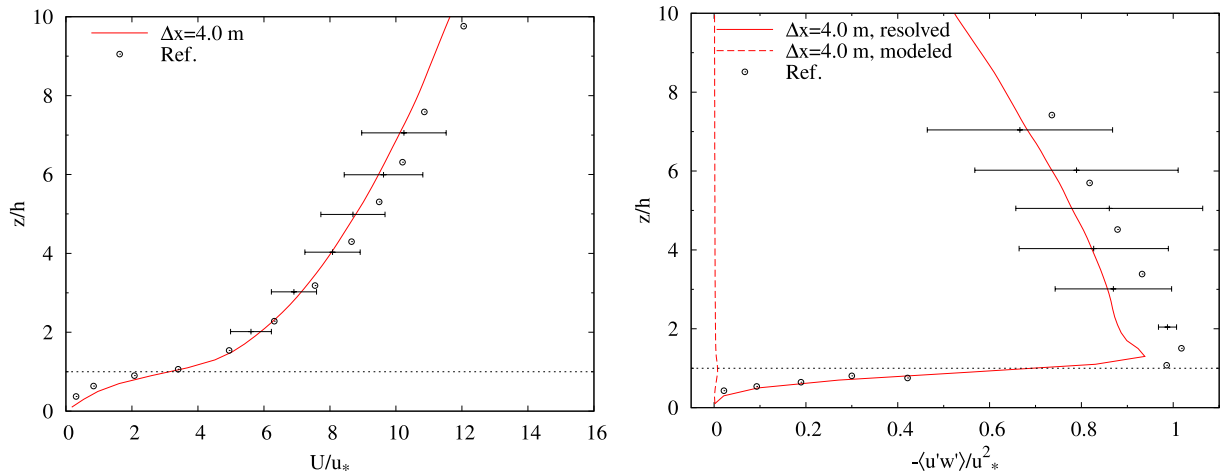

Figure 9. Mean longitudinal velocity profile (left) and resolved and modeled turbulent shear stress (right) predicted by the present LB-LES method in neutral boundary layer with canopy effect. The reference data in (Nebenführ & Davidson, 2015) are denoted by symbols. LB, lattice Boltzmann; LES, large-eddy simulation.

initial temperature is uniform, with $\theta = 300$ K. Lateral boundaries are periodic, a free slip condition with a sponge layer of thickness 50 m is imposed on the top boundary, and while bottom boundary is assumed to be adiabatic with Monin-Obukhov relationships for velocity. The simulations were performed over 3 h of physical time, and results were averaged over the last hour. A uniform grid with $\Delta x = 4$m with $\Delta t = 0.03$ s as applied in the simulation within the canopy.

Results for the neutral case are displayed in Figure 9. The field measurements uncertainties are represented with error bars. Note that the lowest field measurements were taken at $z/h \approx 2$; therefore, the results are normalized with friction velocity calculated at the same height, that is,

$$u_* = \left(\langle u'w'\rangle^2 + \langle v'w'\rangle^2\right)^{1/4}$$

A very good agreement is observed on both the mean velocity profile and the resolved shear stress profile.

Results obtained in the convective and stable cases are shown in Figures 10 and 11, respectively. The velocity profiles exhibit a good agreement with field measurements and simulations for the convective case, and also show an excellent agreement for the stable case. It is worth noting that the stable case shows however smaller velocities above the canopy.

Resolved and modeled vertical momentum fluxes in convective and stable ABL with canopy effects are also presented in Figures 10 and 11, respectively. Results are within the range of field measurements above $z/h = 3$ but deviate at $z/h = 2$.

The resolved turbulent vertical heat flux is shown in Figure 12. An excellent agreement between the present results and reference data is obtained both in convective case and stable case. In general, the present simulations give smaller values on the resolved flux in top region for stable ABL, phenomena that might be due to the use of a sponge layer to prevent the growth of spurious wiggles and waves.

5. Benchmarking: Complex Urban Flows

The last illustrations of the capabilities of the present LBM-LES simulation tool deal with urban flows in complex geometries. The first case deals with the prediction of wind in realistic urban areas, while the second is related to atmospheric dispersion of pollutant in urban areas.

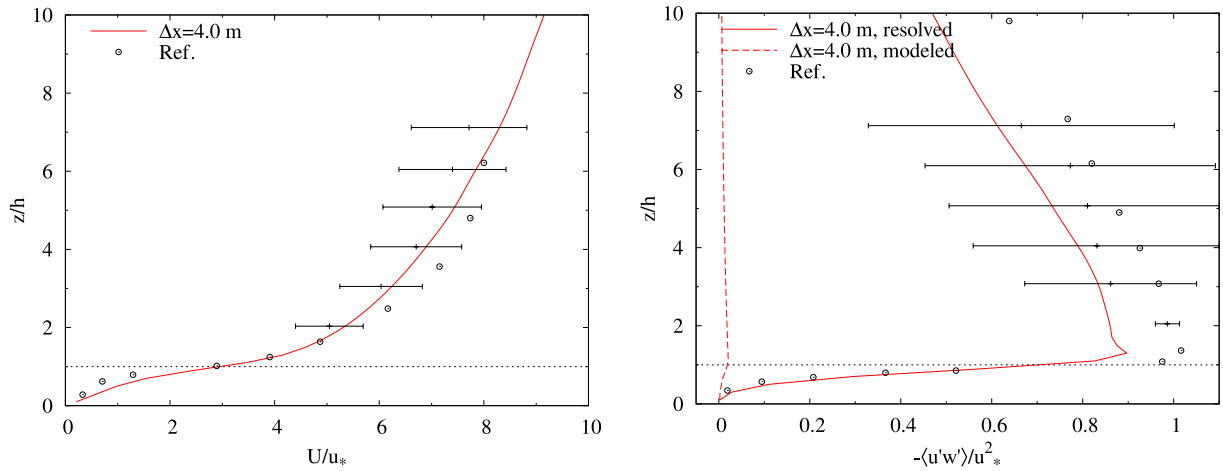

Figure 10. Mean longitudinal velocity profile (left) and resolved and modeled turbulent shear stress (right) predicted by the present LB-LES method in convective boundary layer with canopy effect. The reference data in (Nebenführ & Davidson, 2015) are denoted by symbols. LB, lattice Boltzmann; LES, large-eddy simulation.

5.1. Wind Prediction in Shinjuku District in Tokyo

The first test case for urban flow prediction deals with the prediction of urban wind conditions, including wind gusts for evaluation of pedestrian comfort in the Shinjuku district in Tokyo (Jacob & Sagaut, 2018).

This configuration belongs to the data basis of the Architectural Institute of Japan. An area of 1 km^2 is selected, including all buildings, in which mean wind field measurements are available for the sake of validation. The case of North wind is selected for the sake of illustration.

A computational domain of size 4,600 × 5,000 × 1,500 m is defined. Different grid resolutions have been considered. In the coarse grid, medium and fine grid cases, the smallest mesh size near solid surfaces is taken equal to 2, 1 and 0.5 m, respectively. The total number of grid points ranges from 22×10^6 (coarse grid) to 136×10^6 (fine grid) with a value of 54×10^6 for the medium grid case.

Location of probes used for field measurements and comparisons with LBM-LES results are displayed in Figure 13, showing that at all probe locations (except one) numerical results are within measurement uncertainties.

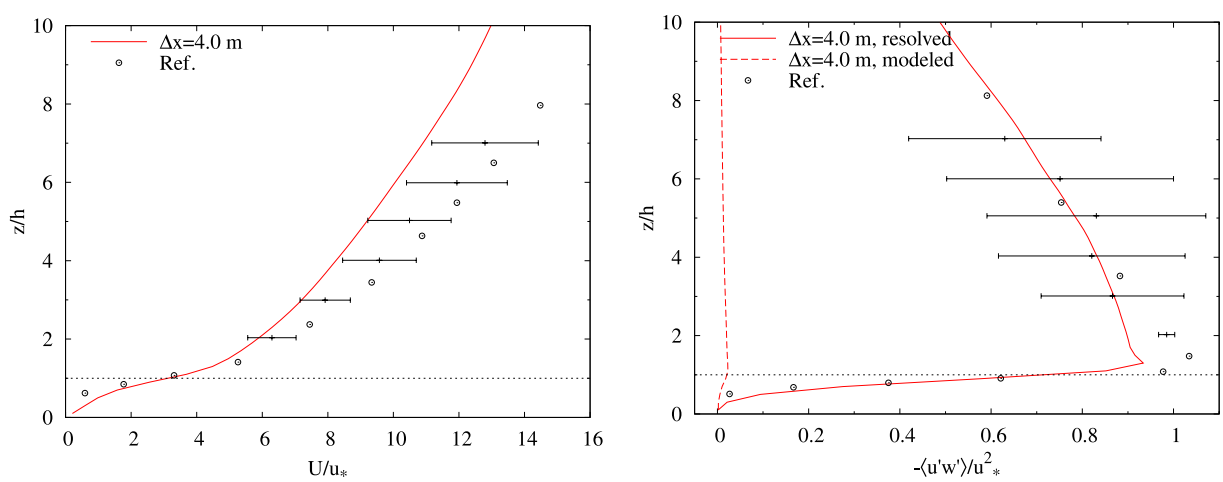

Figure 11. Mean longitudinal velocity profile (left) and resolved and modeled turbulent shear stress (right) predicted by the present LB-LES method in stable boundary layer with canopy effect. The reference data in (Nebenführ & Davidson, 2015) is denoted by symbols. LB, lattice Boltzmann; LES, large-eddy simulation.

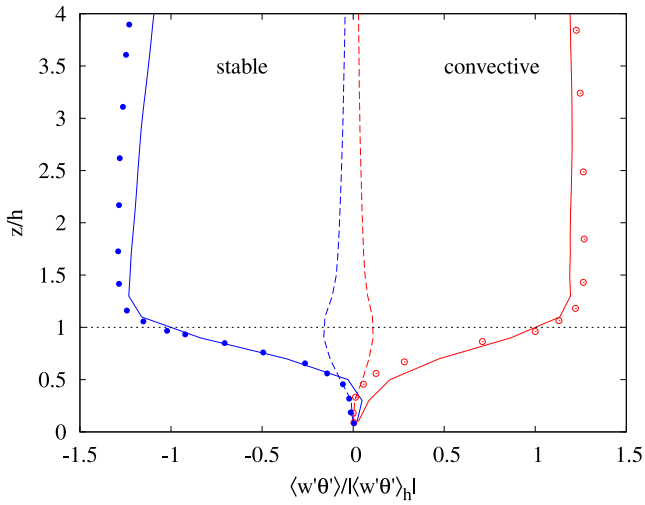

Figure 12. Resolved vertical heat flux (convective and stable canopy). The reference data in (Nebenführ & Davidson, 2015) is denoted by symbols and solid lines represent resolved vertical heat flux and dash lines represent the modeled part.

5.2. Pollutant Dispersion in Paris

The capability of the LBM-LES tool to predict the dispersion of a gaseous pollutant in complex urban areas is now illustrated. For the sake of validation, the MODITIC data basis is used (Merlier et al., 2019; Robins et al., 2016).

The present configuration corresponds to the dispersion of a neutral gas released on the ground at a constant rate in the "Avenue des Champs Elysées" district in Paris, for which wind tunnel data have been produced. The main wind direction and the pollutant source location are shown in Figure 14, and results shown here are related to Configuration 1. The smallest mesh size is taken equal to $H/45$, where H is the mean building height, leading to a total number of grid points equal to 175×10^6 for the configuration 1.

The normalized mean pollutant concentration obtained in both wind tunnel experiments and LBM-LES simulations are displayed in Figure 15. It is observed that very satisfactory results are obtained, including in small streets crossing the main avenue. This last observation shows that a reliable prediction of transverse diffusion in urban areas is obtained.

6. Conclusion

We have described a new tool for LES of atmospheric flows in this paper. LES with the LBM was used to simulate dry and cloudy ABLs, along with flows in complex urban areas. The subgrid model for the LES was the classical Smagorinsky model with a given constant. For dry ABL we used mass, momentum, and potential temperature as governing equations, whereas for cloudy ABL, in addition to mass and momentum, we used liquid and vapor water specific humidities and potential temperature equations. Total water specific humidity is the sum of water vapor and liquid water humidities, and condensation occurs when total water exceeds saturation value. Governing equations were solved by the LBM and by using a finite volume scheme for potential temperature and water specific humidities.

To validate our LBM-LES solver, we first simulated the four basic ABL cases coming from previous intercomparison of LES codes. These were the neutral (Andren et al., 1994; Chow et al., 2005; Senocak et al., 2007), convective (Nieuwstadt et al., 1993; Schmidt & Schumann, 1989), stable (Beare & Macvean, 2004; Beare et al., 2006), and cloudy convective boundary layer (P. Siebesma et al., 2003). Then three extra cases for ABL with canopy effects were performed by our solver. The altitude-dependent drag force and heat release source term were introduced and assessed in the present solver compared reference data in (Nebenführ & Davidson, 2015).

For the neutral case, Coriolis force was added to the LBM, and simulations were performed with $\Delta x = 16$ m and $\Delta x = 32$ m meshes. This case was very sensitive to subgrid model, and only results with subgrid model were satisfactory and presented in the paper. Mean velocity profile, friction velocity and Reynolds stresses predicted in our simulations were in good agreement with literature results. For the convective case, we performed the numerical simulation on $\Delta x = 25$ m and $\Delta x = 50$ m grids with subgrid model. Average temperature profile with subgrid model shows very good agreement with literature results. For stable boundary layer, we used $\Delta x = 3.125$ m, $\Delta x = 6.25$ m, and $\Delta x = 12.5$ m meshes with subgrid model. Mean velocity profile were well reproduced the supergeostrophic jet typical of stable layers. The mean profile of velocity and temperature were in a good agreement with references values.

In assessment of condensation scheme and interaction of forcing terms: condensation, large-scale forcing, a low-level drying, and radiative cooling, the cumulus cloud case was considered by the LBM-LES solver. Very good agreement was obtained for mean velocity, liquid water potential temperature, and vapor water specific humidity on $\Delta x = 40$ m and $\Delta x = 80$ m meshes with subgrid model. Liquid water

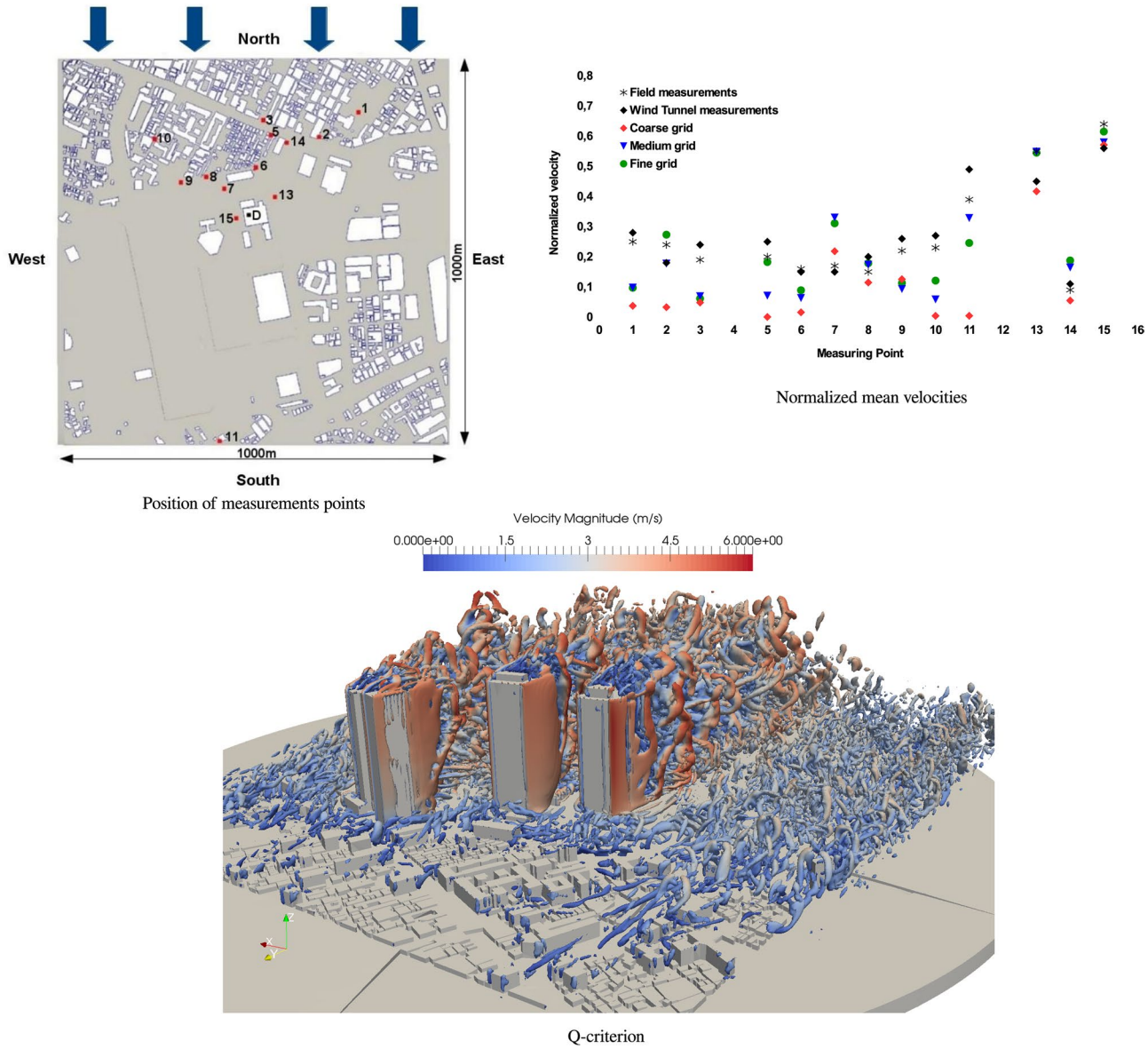

Figure 13. Locations of the probes inside Tokyo Shinjuku district used for in situ field measurements (top-left), simulated normalized velocities compared with wind tunnel and fields measurements (top-right). and complex flow structure illustrated by Q-criterion (bottom).

compares very good to the reference result on the finer mesh, but yields pretty small values on the coarser mesh.

The present LBM-LES method was further assessed considering the flows in neutral, stable and convective boundary layer over a forest canopy. The forest was modeled as a nonuniform homogenized porous medium and implemented as a volumetric source term in both the macroscopic momentum and temperature equations. In general, excellent agreements between the present results and reference data were obtained in neutral convective case and stable ABLs with forest canopy effects.

At last, the LBM-LES tool was successfully assessed considering two urban flow configurations: wind prediction in Shinjuku district in Tokyo, and gaseous pollutant dispersion in the Champs Elysées district in Paris. In both cases, very satisfactory comparisons with experimental data were recovered.

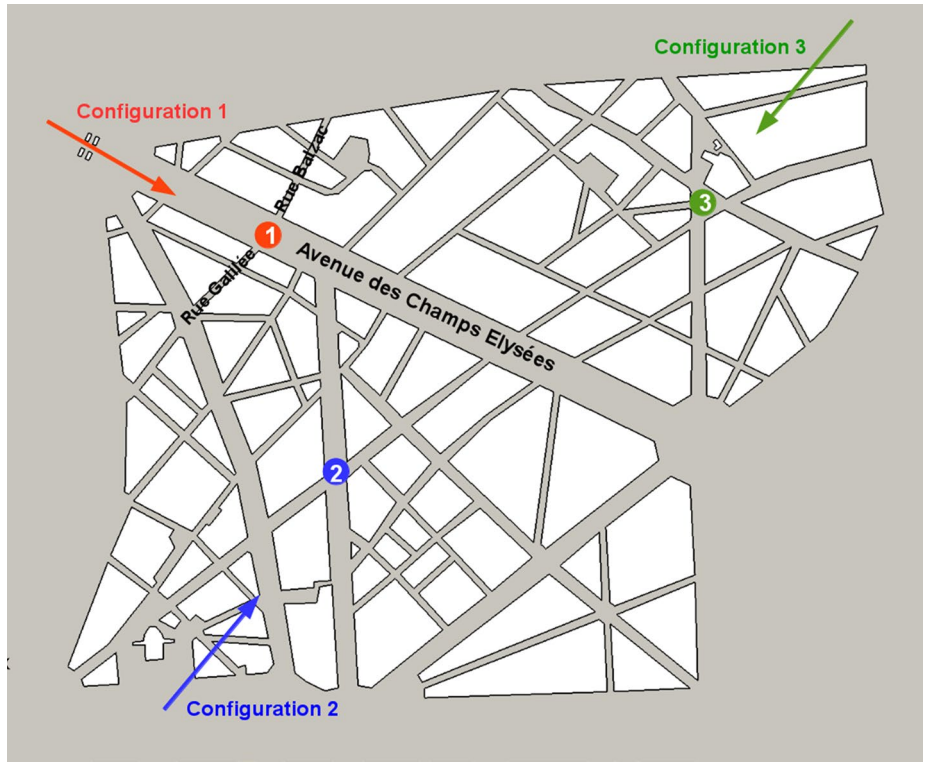

Figure 14. Visualization of the simulated area around the "Avenue des Champs Elysées." Configuration 1 is selected in the present article.

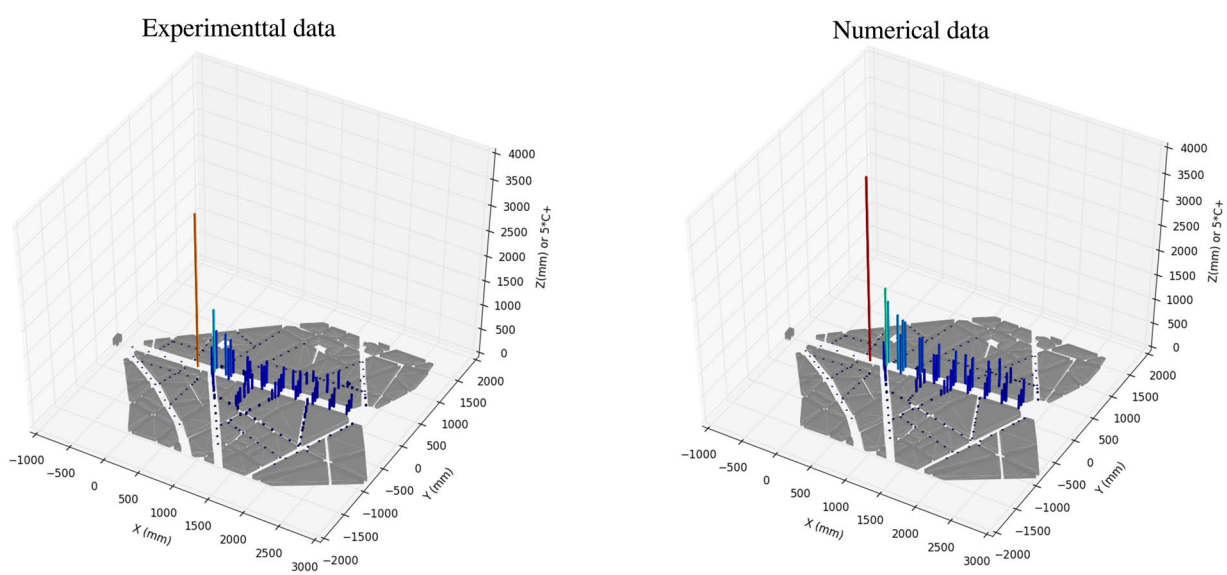

Figure 15. Visualization of the normalized concentration obtained for dispersion of a neutral gas around the "Avenue des Champs Elysées.".

Appendix: Condensation model by invariant variables: 1eq model

Governing equations and condensation model based on two invariant variables (mass fraction of total water q_t and liquid water potential temperature θ_l) are alternatively used and denoted as 1eq model. Equations 4b and 4c can be combined to cancel the source term $\dot{Q}$ in a

$$q_t = q_v + q_l \tag{A.1}$$

conservation equation, becoming

$$\frac{\partial q_t}{\partial t} + u_\alpha \frac{\partial q_t}{\partial x_\alpha} = \frac{\partial}{\partial x_\alpha}\left(D_q \frac{\partial q_t}{\partial x_\alpha} - \overline{q_t' u_i'} \right). \tag{A.2}$$

It then become more convenient to rewrite the energy conservation equation using an approximate expression of the liquid water potential temperature

$$\theta_l \approx \theta - \frac{L_v}{c_p \Pi} q_l, \tag{A.3}$$

to read

$$\frac{\partial \theta_l}{\partial t} + u_\alpha \frac{\partial \theta_l}{\partial x_\alpha} = \frac{\partial}{\partial x_\alpha}\left(D_\theta \frac{\partial \theta_l}{\partial x_\alpha} - \overline{\theta_l' u_i'} \right), \tag{A.4}$$

thereby canceling the source term. Where required, q_l can then be computed from q_t as

$$q_l = \max(0, q_t - q_s). \tag{A.5}$$

In that framework, however, q_s cannot be evaluated directly from Equation 5, as T is not available. It is instead approximated from

$$q_s = q^* \frac{1 + \eta q_t}{1 + \eta q^*}, \quad \eta = \epsilon \frac{L_v^2}{c_p R_d T_l^2}, \tag{A.6}$$

where q^* corresponds to Equation 5, evaluated at $T = \Pi.\theta_l$, rather than $\Pi.\theta$. Compared to the former approach, only two equations of invariant variables (θ_l, q_t) need to be solved in the reduced model, and the relaxation step is replaced by a recovery procedure, which is performed using the approximate expression of saturation humidity following Equation (A.6). In the same approach, the subgrid fluxes are expressed as

$$\overline{\theta_l' u_j'} = -D_{h,t} \frac{\partial \theta_l}{\partial x_j}, \tag{A.7a}$$

$$\overline{q_t' u_j'} = -D_{q,t} \frac{\partial q_t}{\partial x_j} \tag{A.7b}$$

Data Availability Statement

Primary data and scripts used in this study are stored in public repository (https://www.researchgate.net/publication/339901171_data_ProLB_ABL) with an individual DOI number 10.13140/RG.2.2.27679.10400.

Acknowledgments
This work was granted access to the HPC resources of Aix-Marseille Université financed by the project Equip@Meso (ANR-10-EQPX-29-01) of the program "Investissements d'Avenir" supervised by the Agence Nationale de la Recherche. This work was performed using HPC resources from GENCI-TGCC/CINES (Grant 2018-A0052A07679). This work was also supported by project of ProLB software (http://www.prolb-cfd.com). The ProLB solver is available under the ProLB Software License Agreement of CS Communication & Systemes (http://www.prolb-cfd.com/licensing-and-services/).

References

Ahmad, N. H., Inagaki, A., Kanda, M., Onodera, N., & Aoki, T. (2017). Large-eddy simulation of the gust index in an urban area using the lattice Boltzmann method. *Boundary-Layer Meteorology*, *163*(3), 447–467.

Andren, A., Brown, A. R., Mason, P. J., Graf, J., Schumann, U., Moeng, C.-H., & Nieuwstadt, F. T. M. (1994). Large-eddy simulation of a neutrally stratified boundary layer: A comparison of four computer codes. *Quarterly Journal of the Royal Meteorological Society*, *120*(520), 1457–1484. https://doi.org/10.1002/qj.49712052003

Banerjee, T., De Roo, F., & Mauder, M. (2017). Explaining the convector effect in canopy turbulence by means of large-eddy simulation. *Hydrology and Earth System Sciences*, *21*(6), 2987–3000. https://doi.org/10.5194/hess-21-2987-2017

Bartlett, C., Chen, H., Staroselsky, I., Wanderer, J., & Yakhot, V. (2013). Lattice Boltzmann two-equation model for turbulence simulations: High-Reynolds number flow past circular cylinder. *International Journal of Heat and Fluid Flow*, *42*, 1–9.

Beare, R. J., & Macvean, M. K. (2004). Resolution sensitivity and scaling of large-eddy simulations of the stable boundary layer. *Boundary-Layer Meteorology*, *112*(2), 257–281.

Beare, R. J., Macvean, M. K., Holtslag, A. A. M., Cuxart, J., Esau, I., Golaz, J.-C., et al. (2006). An intercomparison of large-eddy simulations of the stable boundary layer. *Boundary-Layer Meteorology*, *118*(2), 247–272. https://doi.org/10.1007/s10546-004-2820-6

Blocken, B. (2015). Computational fluid dynamics for urban physics: Importance, scales, possibilities, limitations and ten tips and tricks toward accurate and reliable simulations. *Building and Environment*, *91*, 219–245.

Chateau, S., Favier, J., D'Ortona, U., & Poncet, S. (2017). Transport efficiency of metachronal waves in 3d cilium arrays immersed in a two-phase flow. *Journal of Fluid Mechanics*, *824*, 931–961.

Chen, S., & Doolen, G. D. (1998). Lattice Boltzmann method for fluid flows. *Annual Review of Fluid Mechanics*, *30*(1), 329–364.

Chen, H., Orszag, S. A., Staroselsky, I., & Succi, S. (2004). Expanded analogy between Boltzmann kinetic theory of fluids and turbulence. *Journal of Fluid Mechanics*, *519*, 301–314.

Chevillotte, F., & Ricot, D. (2016). *Development and evaluation of non-reflective boundary conditions for lattice Boltzmann method*. Paper presented at 22nd AIAA/CEAS Aeroacoustics Conference (p. 2915).

Cheylan, I., Fritz, G., Ricot, D., & Sagaut, P. (2019). Shape optimization using the adjoint lattice Boltzmann method for aerodynamic applications. *AIAA Journal*, 1–16.

Chow, F. K., Street, R. L., Xue, M., & Ferziger, J. H. (2005). Explicit filtering and reconstruction turbulence modeling for large-eddy simulation of neutral boundary layer flow. *Journal of the Atmospheric Sciences*, *62*(7), 2058–2077.

Coreixas, C., Wissocq, G., Puigt, G., Boussuge, J.-F., & Sagaut, P. (2017). Recursive regularization step for high-order lattice Boltzmann methods. *Physical Review E*, *96*(3), 033306.

Cushman-Roisin, B., & Beckers, J.-M. (2009). *Introduction to geophysical fluid dynamics: Physical and numerical aspects*. Academic Press.

Deardorff, J. (1980). Stratocumulus-capped mixed layer derived from a three-dimensional model. *Boundary-Layer Meteorology*, *18*, 495–527.

Dipankar, A., Stevens, B., Heinze, R., Moseley, C., Zängl, G., Giorgetta, M., & Brdar, S. (2015). Large eddy simulation using the general circulation model icon. *Journal of Advances in Modeling Earth Systems*, *7*(3), 963–986. https://doi.org/10.1002/2015MS000431

Dyer, A. J. (1974). A review of flux-profile relationships. *Boundary-Layer Meteorology*, *7*(3), 363–372. https://doi.org/10.1007/BF00240838

d'Humières, D., Ginzburg, I., Krafczyk, M., Lallemand, P., & Luo, L.-S. (2002). Multiple-relaxation-time lattice Boltzmann models in three dimensions. *Philosophical Transactions of the Royal Society of London - A*, *360*, 437–451.

D'humières, D., & Lallemand, P. (1986). Lattice gas automata for fluid mechanics. *Physica A: Statistical Mechanics and Its Applications*, *140*(1–2), 326–335.

Eggels, J. G. (1996). Direct and large-eddy simulation of turbulent fluid flow using the lattice-Boltzmann scheme. *International Journal of Heat and Fluid Flow*, *17*(3), 307–323. http://dx.doi.org/10.1016/0142-727X(96)00044-6

Feng, Y., Boivin, P., Jacob, J., & Sagaut, P. (2019a). Hybrid recursive regularized lattice Boltzmann simulation of humid air with application to meteorological flows. *Physical Review E*, *100*(2), 023304.

Feng, Y., Guo, S., Jacob, J., & Sagaut, P. (2019b). Solid wall and open boundary conditions in hybrid recursive regularized lattice Boltzmann method for compressible flows. *Physics of Fluids*, *31*, 126103.

Fernando, H., Lee, S., Anderson, J., Princevac, M., Pardyjak, E., & Grossman-Clarke, S. (2001). Urban fluid mechanics: Air circulation and contaminant dispersion in cities. *Environmental Fluid Mechanics*, *1*(1), 107–164.

Gao, T., Tseng, Y.-H., & Lu, X.-Y. (2007). An improved hybrid Cartesian/immersed boundary method for fluid–solid flows. *International Journal for Numerical Methods in Fluids*, *55*(12), 1189–1211.

Geier, M. (2008). De-aliasing and stabilization formalism of the cascaded lattice Boltzmann automaton for under-resolved high Reynolds number flow. *International Journal for Numerical Methods in Fluids*, *56*, 1249–1254.

Geier, M., Greiner, A., & Korvink, J. (2006). Cascaded digital lattice Boltzmann automata for high Reynolds number flow. *Physical Review E - Statistical Physics, Plasmas, Fluids, and Related Interdisciplinary Topics*, *73*, 066705.

Heerwaarden, C. C. v., Van Stratum, B. J., Heus, T., Gibbs, J. A., Fedorovich, E., & Mellado, J. P. (2017). MicroHH 1.0: A computational fluid dynamics code for direct numerical simulation and large-eddy simulation of atmospheric boundary layer flows. *Geoscientific Model Development*, *10*(8), 3145–3165.

Hirsch, C. (2007). *Numerical computation of internal and external flows: The fundamentals of computational fluid dynamics*. Elsevier.

Hou, S., Sterling, J., Chen, S., & Doolen, G. (1994). A lattice Boltzmann subgrid model for high Reynolds number flows. *arXiv Preprint Comp-Gas/9401004*.

Jacob, J., Malaspinas, O., & Sagaut, P. (2018). A new hybrid recursive regularised Bhatnagar–Gross–Krook collision model for lattice Boltzmann method-based large eddy simulation. *Journal of Turbulence*, *19*(11–12), 1051–1076.

Jacob, J., & Sagaut, P. (2018). Wind comfort assessment by means of large eddy simulation with lattice Boltzmann method in full scale city area. *Building and Environment*, *139*, 110–124.

Kim, K. H., Kim, C., & Rho, O.-H. (2001). Methods for the accurate computations of hypersonic flows: I. AUSMPW+ scheme. *Journal of Computational Physics*, *174*(1), 38–80.

Latt, J., & Chopard, B. (2006). Lattice Boltzmann method with regularized pre-collision distribution functions. *Mathematics and Computers in Simulation*, *72*, 165–168.

Malaspinas, O. (2015). Increasing stability and accuracy of the lattice Boltzmann scheme: Recursivity and regularization. *ArXiv E-Prints*.

Malaspinas, O., & Sagaut, P. (2011). Advanced large-eddy simulation for lattice Boltzmann methods: The approximate deconvolution model. *Physics of Fluids*, *23*(10), 105103.

Malaspinas, O., & Sagaut, P. (2012). Consistent subgrid scale modelling for lattice-Boltzmann methods. *Journal of Fluid Mechanics*, *700*, 514–542.

Markkanen, T., Rannik, Ü., Marcolla, B., Cescatti, A., & Vesala, T. (2003). Footprints and fetches for fluxes over forest canopies with varying structure and density. *Boundary-Layer Meteorology*, *106*(3), 437–459. https://doi.org/10.1023/A:1021261606719

Maronga, B., Gryschka, M., Heinze, R., Hoffmann, F., Kanani-Sühring, F., Keck, M., et al. (2015). The parallelized large-eddy simulation model (palm) version 4.0 for atmospheric and oceanic flows: Model formulation, recent developments, and future perspectives. *Geoscientific Model Development Discussions*, *8*(2015), 1539–1637.

Mattila, K. K., Philippi, P. C., & HegeleJr, L. A. (2017). High-order regularization in lattice-Boltzmann equations. *Physics of Fluids*, *29*(4), 046103. https://doi.org/10.1063/1.4981227

Merlier, L., Jacob, J., & Sagaut, P. (2019). Lattice-Boltzmann large-eddy simulation of pollutant dispersion in complex urban environment with dens gas effects: Model evaluation and flow analysis. *Building and Environment*, *148*, 634–652.

Moeng, C. (1984). A large-eddy-simulation model for the study of planetary boundary-layer turbulence. *Journal of the Atmospheric Sciences*, *41*, 2052–2062.

Nebenführ, B., & Davidson, L. (2015). Large-eddy simulation study of thermally stratified canopy flow. *Boundary-Layer Meteorology*, *156*(2), 253–276. https://doi.org/10.1007/s10546-015-0025-9

Nieuwstadt, F. T., Mason, P. J., Moeng, C.-H., & Schumann, U. (1993). Large-eddy simulation of the convective boundary layer: A comparison of four computer codes. Turbulent shear flows. Vol. 8 (pp. 343–367). Springer.

Premnath, K. N., & Banerjee, S. (2011). On the three-dimensional central moment lattice Boltzmann method. *Journal of Statistical Physics*, *143*(4), 747–794.

Premnath, K. N., Pattison, M. J., & Banerjee, S. (2009a). Dynamic subgrid scale modeling of turbulent flows using lattice-Boltzmann method. *Physica A: Statistical Mechanics and Its Applications*, *388*(13), 2640–2658. http://dx.doi.org/10.1016/j.physa.2009.02.041

Premnath, K. N., Pattison, M. J., & Banerjee, S. (2009b). Generalized lattice Boltzmann equation with forcing term for computation of wall-bounded turbulent flows. *Physical Review E - Statistical Physics, Plasmas, Fluids, and Related Interdisciplinary Topics*, *79*, 026703. https://doi.org/10.1103/PhysRevE.79.026703

Pressel, K. G., Kaul, C. M., Schneider, T., Tan, Z., & Mishra, S. (2015). Large-eddy simulation in an anelastic framework with closed water and entropy balances. *Journal of Advances in Modeling Earth Systems*, *7*(3), 1425–1456.

Prusa, J. M., Smolarkiewicz, P. K., & Wyszogrodzki, A. A. (2008). Eulag, a computational model for multiscale flows. *Computers & Fluids*, *37*(9), 1193–1207.

Qian, Y., d'Humières, D., & Lallemand, P. (1992). Lattice BGK models for Navier-Stokes equation. *Europhysics Letters*, *17*(6), 479–484.

Robins, A., Hayden, P., & Wingstedt, E. M. M. (2016). *MODITIC wind tunnel experiments, Tech. Rep. FFI-RAPPORT 16/01483*. Norwegian Defence Research Establishment.

Sagaut, P. (2006). *Large eddy simulation for incompressible flows: An introduction*. Springer Science & Business Media.

Sagaut, P. (2010). Toward advanced subgrid models for lattice-Boltzmann-based large-eddy simulation: Theoretical formulations. *Computers & Mathematics with Applications*, *59*(7), 2194–2199.

Schmidt, H., & Schumann, U. (1989). Coherent structure of the convective boundary layer derived from large-eddy simulations. *Journal of Fluid Mechanics*, *200*, 511–562.

Senocak, I., Ackerman, A. S., Kirkpatrick, M. P., Stevens, D. E., & Mansour, N. N. (2007). Study of near-surface models for large-eddy simulations of a neutrally stratified atmospheric boundary layer. *Boundary-Layer Meteorology*, *124*(3), 405–424. https://doi.org/10.1007/s10546-007-9181-x

Shepard, D. (1968). A two-dimensional interpolation function for irregularly-spaced data. *Proceedings of the 1968 23rd ACM national conference* (pp. 517–524) ACM.

Siebesma, A. P., Bretherton, C. S., Brown, A., Chlond, A., Cuxart, J., Duynkerke, P. G., et al. (2003). A large eddy simulation intercomparison study of shallow cumulus convection. *Journal of the Atmospheric Sciences*, *60*(10), 1201–1219. https://doi.org/10.1175/1520-0469(2003)60<1201:ALESIS>2.0.CO;2

Siebesma, A., & Cuijpers, J. (1995). Evaluation of parametric assumptions for shallow cumulus convection. *Journal of the Atmospheric Sciences*, *52*(6), 650–666.

Sommeria, G. (1976). Three-dimensional simulation of turbulent processes in an undisturbed trade wind boundary layer. *Journal of the Atmospheric Sciences*, *33*, 216–241.

Stevens, B., Moeng, C.-H., Ackerman, A. S., Bretherton, C. S., Chlond, A., de Roode, S., et al. (2005). Evaluation of large-eddy simulations via observations of nocturnal marine stratocumulus. *Monthly Weather Review*, *133*(6), 1443–1462.

Succi, S. (2020). Toward a self-consistent Boltzmann's kinetic model of fluid turbulence. *Journal of Turbulence*, *21*(7), 375–385. https://doi.org/10.1080/14685248.2020.1797060

Teixeira, C. M. (1998). Incorporating turbulence models into the lattice-Boltzmann method. *International Journal of Modern Physics C*, *9*(08), 1159–1175.

Wilhelm, S., Jacob, J., & Sagaut, P. (2018). An explicit power-law-based wall model for lattice-Boltzmann-method-Reynolds-averaged numerical simulations of the flow around airfoils. *Physics of Fluids*, *30*, 065111.

Wilhelm, S., Jacob, J., & Sagaut, P. (2020). A new explicit algebraic wall model for les of turbulent flows under adverse pressure gradient. *Flow, Turbulence and Combustion*, *106*, 1–35.

Xu, H., & Sagaut, P. (2013). Analysis of the absorbing layers for the weakly-compressible lattice Boltzmann methods. *Journal of Computational Physics*, *245*, 14–42.

Yu, H., Luo, L.-S., & Girimaji, S. S. (2006). LES of turbulent square jet flow using an MRT lattice Boltzmann model. *Computers & Fluids*, *35*(8), 957–965.

Zhang, R., Fan, H., & Chen, H. (2011). A lattice Boltzmann approach for solving scalar transport equations. *Philosophical Transactions of the Royal Society of London - A: Mathematical, Physical and Engineering Sciences*, *369*(1944), 2264–2273.